International Journal of Pharmaceutics 652 (2024) 123821

Contents lists available at ScienceDirect

International Journal of Pharmaceutics

journal homepage: www.elsevier.com/locate/ijpharm

Combinational antimicrobial activity of biogenic TiO_2 NP/ZnO NPs nanoantibiotics and amoxicillin-clavulanic acid against MDR-pathogens

Mina Masoudi [a,b], Mansour Mashreghi [b,c,d,*], Alireza Zenhari [b], Amirala Mashreghi [e]

[a] Department of Pathobiology, Faculty of Veterinary Medicine, Ferdowsi University of Mashhad, Mashhad, Iran
[b] Department of Biology, Faculty of Science, Ferdowsi University of Mashhad, Mashhad, Iran
[c] Industrial Biotechnology Research Group, Institute of Biotechnology, Ferdowsi University of Mashhad, Mashhad, Iran
[d] Nano Research Center, Ferdowsi University of Mashhad, Mashhad, Iran
[e] Faculty of Medicine, Mashhad University of Medical Sciences, Mashhad, Iran

ARTICLE INFO

Keywords:
Nanoantibiotics
Amoxicillin-clavulanic acid
Metal oxide nanoparticles
Antibacterial activity
Multidrug-resistant pathogens

ABSTRACT

The development of effective strategies against multidrug-resistant (MDR) pathogens is an urgent need in modern medicine. Nanoantibiotics (nABs) offer a new hope in countering the surge of MDR-pathogens. The aim of the current study was to evaluate the antibacterial activity of two attractive nABs, TiO_2 NPs and ZnO NPs, and their performance in improving the antimicrobial activity of defined antibiotics (amoxicillin-clavulanic acid, amox-clav) against MDR-pathogens. The nABs were synthesized using a green method. The physicochemical characteristics of the synthesized nanoparticles were determined using standard methods. The results showed the formation of pure anatase TiO_2 NPs and hexagonal ZnO NPs with an average particle size of 38.65 nm and 57.87 nm, respectively. The values of zeta potential indicated the high stability of the samples. At 8 mg/mL, both nABs exhibited 100 % antioxidant activity, while ZnO showed significantly higher activity at lower concentrations. The antibiofilm assay showed that both nABs could inhibit the formation of biofilms of *Acinetobacter baumannii* 80 and *Escherichia coli* 27G (MDR-isolates). However, ZnO NPs showed superior antibiofilm activity (100 %) against *E. coli* 27G. The MIC values were determined to be 8 (1), 2 (2), and 4 (4) mg/mL for amox-clav, TiO_2 NPs, and ZnO NPs against *A. baumannii* 80 (*E. coli* 27G), respectively. The results showed that both nABs had synergistically enhanced antibacterial performance in combination with amox-clav. Specifically, an 8-fold reduction in MIC values of antibiotics was observed when they were combined with nABs. These findings highlight the potential of TiO_2 NPs and ZnO NPs as effective nanoantibiotics against MDR-pathogens. The synergistic effect observed when combining nABs with antibiotics suggests a promising approach for combating antibiotic resistance. Further research and development in this area could lead to the development of more effective treatment strategies against MDR infections.

1. Introduction

Antibiotic-resistant pathogens are serious health crises in modern medicine, resulting in 3500 deaths caused by human chronic infectious diseases (Uyttebroek et al., 2022). The high cost and the murky profit model associated with the development of new antibiotics have urged scientists to seek alternative strategies. Recent advances in nanomaterial-based antimicrobial agents provide new opportunities to address antibiotic-resistant pathogens (Makabenta et al., 2021). Nanomaterials that either exhibit antimicrobial activity on their own or improve the efficacy and safety of antibiotics administration are referred to as nanoantibiotics (nABs) (Teixeira et al., 2020). Compared to conventional antibiotics, nABs offer several advantages including low cost, low immunosuppression, low antimicrobial resistance, low side effects, better solubility, targeted delivery, controlled release, prolonged therapeutic effect by slow elimination as well as adaptability for the resistant antimicrobial world (Thangadurai et al., 2020).

In recent years, significant efforts have been committed to developing novel nABs as an alternative and long-term solution for antimicrobial drug resistance. nABs typically consist of metal, metal oxides, or their composites (Uzair et al., 2020; Alabdali et al., 2022). Metal oxide nanoparticles (MNPs) with well-defined sizes and variable surface chemistry are emerging as the next-generation effective nABs. The antibacterial activity of MNPs begins with their direct contact with the

* Corresponding author.
E-mail address: mashrghi@um.ac.ir (M. Mashreghi).

https://doi.org/10.1016/j.ijpharm.2024.123821
Received 4 September 2023; Received in revised form 12 January 2024; Accepted 16 January 2024
Available online 17 January 2024

bacterial cell walls, bypassing the need to penetrate the cells. This mechanism allows MNPs to evade existing resistance mechanisms and makes them less prone to selecting for resistance compared to conventional antibiotics (Fernando et al., 2018). The physicochemical characteristics of MNPs including size, shape, and surface chemistry play a crucial role in their therapeutic activities (Kiio and Park, 2021). These characteristics affect the antibacterial properties of MNPs by catalyzing the bacterial intracellular biochemical processes. The synthesis method of MNPs is reported as a key factor in determining the properties of the end products (Nyoka et al., 2020). However, there is a concern about the introduction of toxic materials used in the synthesis of MNPs into the environment (Hano and Abbasi, 2021). As a result, green synthesis methods have gained attention because of their safety, biocompatibility, and environmental friendliness (Hano and Abbasi, 2021).

MNPs including CuO, Au, Ag, TiO_2, and ZnO nanoparticles, have been studied for their potential as alternative antimicrobial agents against various pathogens (Ovais et al., 2019; Lv et al., 2023; Rajput et al., 2023). Among these, TiO_2 NPs and ZnO NPs are particularly important due to their wide biomedical applications and low toxicity (El-Kahky et al., 2021). The US Food and Drug Administration (FDA) has approved the use of TiO_2 NPs and ZnO NPs for some medical products which are in commercial use (Javed et al., 2022; Zare et al., 2022). There has been an increasing number of publications in recent years on the synergistic antibacterial effects between MNPs and antibiotics (Kanwal et al., 2022). The combination of MNPs with antibiotics allows for the use of lower drug doses, which can help decrease side effects, and potentially reduce the evolution of multidrug-resistance mechanisms. While most studies have focused on the synergistic antibacterial activity of silver nanoparticles (Ag NPs) with other nanoparticles or antibiotics (Sajjad et al., 2019; Abbas et al., 2022), there are some reports on the application of TiO_2 NPs and ZnO NPs in combination with antibiotics such as cephalosporins, glycopeptides, azalides, gentamicin, erythromycin, ampicillin, colistin, meropenem, ciprofloxacin, and tetracycline against methicillin-resistant *Staphylococcus aureus* (MRSA), *Acinetobacter baumannii* (*A. baumannii*) and *Escherichia coli* (*E. coli*) bacteria (Fadwa et al., 2021; Vanamala et al., 2021; Ribeiro et al., 2022).

In this study, we evaluate the antibacterial activity of two biogenic nABs in combination with amoxicillin-clavulanic acid (amox-clav) antibiotics against MDR-isolates, including *Acinetobacter baumannii* 80 and *Escherichia coli* 27G. We also investigated the antioxidant and antibiofilm activities, as well as the bacterial cell membrane integrity of the nABs.

2. Materials and methods

2.1. Bacterial strains and culture

The luminescent strain *Vibrio harveyi* VLC was utilized for the synthesis of MNPs specifically TiO_2 NPs and ZnO NPs. Antibiotic resistant strains, *Acinetobacter baumannii* 80 and *Escherichia coli* 27G were isolated from Ghaem hospital in Mashhad, Iran and used for antibacterial and antibiofilm activity assays. The strains were restored from purified glycerol stock stores at −20 ℃. The freezer stocks of bacteria were melted at room temperature and inoculated in sterile nutrient broth (NB) medium. They were then incubated overnight at 37 ℃. A loop of each bacterium was streaked onto nutrient agar (NA) plates and incubated at 37 ℃ for 24 h. A pure colony of bacteria was subcultured in NB medium and used for all microbial assays.

2.2. Antibiotic susceptibility test

To determine the antibiotic-resistant profile of the test bacteria, the Kirby–Bauer disk diffusion assay on Mueller–Hinton agar (MHA) was used (Sreenivasan et al., 2022). The procedure involved placing antibiotic discs on MHA plates that were previously smeared with a bacterial suspension of 0.5 McFarland. The plates were then incubated at 37 °C for 24 h. The antibiotic disks used in this study included: amoxicillin (AMX: 25 μg), cefoxitin (FOX: 30 μg), levofloxacin (LEV: 5 μg), ceftriaxone (CRO: 30 μg), ticarcillin (TIC: 75 μg), amoxicillin-clavulanic acid (AMC: 30 μg), carbenicillin (CB: 100 μg), cefazolin (CZ: 30 μg), ampicillin (AM: 10 μg), cephalexin (CN: 30 μg), imipenem (IPM: 10 μg), piperacillin (PIP: 100 μg), gentamicin (GM: 10 μg), amikacin (AN: 30 μg), ciprofloxacin (CP: 5 μg), trimethoprim-sulfamethoxazole (SXT: 1.25/23.75 μg), nalidixic acid (NA: 30 μg). The inhibition zone (diameter) around each antibiotic disc was measured after the incubation period, and the results were evaluated according to the guidelines set by the Clinical and Laboratory Standards Institute (CLSI) (Weinstein and Lewis, 2020).

2.3. TiO_2 NPs and ZnO NPs biosynthesis and characterization

TiO_2 NPs and ZnO NPs were synthesized using cell lysate supernatant (CLS) of *V. harveyi* VLC as previously reported (Masoudi et al., 2023). Briefly, the synthesis process involved inoculating a single colony of the bacteria into the sterile seawater complete medium (SWC, 2.4 % w/v sea salt, 0.5 % w/v peptone, 0.3 % w/v yeast extract, and 0.3 % v/v glycerol) and incubating it overnight at 28 ℃ with orbital shaking at 150 rpm. The bacterial cells were harvested by centrifugation at 5000 rpm for 10 min and lysed in sterile distilled water (SDW) using sonication for 10 min. The cell-free extract of bacteria was obtained by centrifugation (8000 rpm for 20 min) and used for MNPs synthesis. To obtain TiO_2 NPs and ZnO NPs, 50 mL titanyl hydroxide ($TiO(OH)_2$, 25 mM) and 20 mL of zinc sulfate monohydrate ($ZnSO_4{\cdot}H_2O$, 100 mM) solution were separately added to 100 mL of cell-free extract of bacteria and incubated in a water bath at 100 ℃ for 1 h. The solution containing white precipitate was centrifuged, and the resultant pellet was washed at least three times with SDW and dried using a freeze dryer (Christ, Germany).

The MNPs biosynthesis was first monitored by visual inspection and further confirmed using a UV1700 spectrophotometer (Shimadzu, Japan) within the absorbance range of 200–800 nm, the Fourier transform infrared (FTIR) spectrophotometer (Nicolet Avatar, USA) in the range of 400–4000 cm^{-1} using KBr pellet method, and X-ray diffractometer (XRD) (Bruker, Germany) using Cu K_α X-ray ($\lambda = 0.15406$ nm) as a radiation source and scanning for the range $20^\circ \leq 2\theta \leq 80^\circ$. The shape and size of the samples were examined by Mira 3-XMU high field emission scanning electron microscope (FESEM, TESCAN, Czech Republic) and the PSD (particle size distribution) plots were obtained by determining the size of 50 particles for each sample (using Digimizer 4.0, MedCalc Software, Belgium). Particle size and polydispersity index (PDI) were determined based on dynamic light scattering (DLS) using a VASCO3 particle size analyzer (Cordouan Technologies, France). The zeta potential of dispersed samples in NB medium was determined using a zeta compact (CAD, France) at room temperature.

The presence of protein on the surface of the samples was quantified using the Bradford protein assay (Masoudi et al., 2018). The Bradford reagent (100 μL) was added to different concentrations of the samples (0.25, 0.5, 1, and 2 mg/mL) and the mixture was incubated for 30 min in the dark at room temperature. The optical density (OD) was measured at 630 nm. Bovine serum albumin (BSA) was used as a standard protein and the total protein concentration of the samples was determined by extrapolating the standard curve. Moreover, a Synergy H4 microplate reader (BioTek, USA) was used to record the fluorescence spectra of both samples ($\lambda_{Ex} = 450$ nm).

2.4. Preparation of nanoparticles suspension

Stock suspension of each sample was prepared in NB medium. The samples were stirred for 2 h, then preactivated under UV light (15 W, VL-115.L UV lamp) with a wavelength of 365 nm for 2 h followed by stirring for another 2 h.

2.5. Antibacterial activity

To determine the antibacterial activity of nABs against MDR-isolates (*A. baumannii* 80 and *E. coli* 27G), the minimum inhibitory concentration (MIC), minimum bactericidal concentration (MBC), and colony-forming (CF) assays were performed. The synergistic antibacterial activity of the samples in combination with amoxicillin-clavulanic acid (amox-clav; 14:1) was evaluated using a checkerboard assay.

2.5.1. Determination of minimum inhibitory concentration

The antibacterial activity of biogenic nABs and amox-clav was evaluated at different concentrations (0.015, 0.03, 0.06, 0.12, 0.25, 1, 2, 4, and 8 mg/mL) against *E. coli* ATCC 25922 and MDR-isolates, *A. baumannii* 80 and *E. coli* 27G, using the broth microdilution method (Masoudi et al., 2018). The procedure involved adding 100 μL of NB medium to wells of microplates, followed by the addition of 100 μL of the stock suspension of each sample at the first column. Then, 100 μL of suspension was transferred to the adjacent columns and a serial dilution was performed to make sample concentrations of 8 to 0.015 mg/mL. Afterward, 10 μL of each bacterial suspension (10^8 CFU/mL) was added to each well, except for the wells including negative control (containing only NB medium), and blank (containing NB medium with varying nABs concentrations). The wells containing bacteria inoculum with culture medium without samples were considered as a positive control. The microplates were incubated at 37 °C and the OD at 630 nm was recorded after 20 h using a Stat Fax 2100 microplate reader (Awareness Technology, USA). The minimum inhibitory concentration (MIC) was determined as the lowest concentration of antibacterial agent showing visual inhibition of growth. The percentage of bacterial growth inhibition was determined using the following equations:

$$\text{Bacterial Growth Inhibition}\,(\%) = \left[\frac{\text{OD}_{\text{Positive Control}} - \text{OD}_{\text{Sample}}}{\text{OD}_{\text{Positive Control}}}\right] \times 100$$

$$\text{OD}_{\text{Sample}} = \text{OD}_{\text{Test}} - \text{OD}_{\text{Blank}}$$

2.5.2. Determination of minimum bactericidal concentration

The minimum bactericidal concentration (MBC) was considered to be the minimum concentration of antibacterial agent that reduces the initial concentration of bacteria in the culture to less than 0.1 %, and did not form a single bacterial colony on NA medium (Rossato Viana et al., 2022). The MBC of each sample was determined by subculturing 10 μL of the overnight wells to NA plates and incubating them at 37 ℃ for 24 h.

The colony forming assay (CFA) was performed to evaluate the antibacterial activity of nABs. *A. baumannii* 80 and *E. coli* 27G isolates were inoculated in NB medium containing different concentrations of the samples (1, 2, 4, and 8 mg/mL) at the final concentration of 10^7 CFU/mL. Following incubation for 12 h at 37 ℃, the suspension was diluted 10^6 times, and 100 μL of it was spread on NA plate and incubated at 37 ℃ for 24 h. For control, bacteria were inoculated in NB medium without the nABs. The number of colonies was counted and the number of viable cells was calculated as colony forming per milliliter (CFU/mL) using the following equation:

$$\text{CFU/mL} = \frac{\text{Number of colonies} \times \text{Total dilution factor}}{\text{Volume of culture plated in mL}}$$

The bactericidal rate (K) was also calculated using the following equation:

$$\text{K} = \frac{\text{N}_\text{C} - \text{N}_\text{T}}{\text{N}_\text{C}} \times 100$$

where N_C and N_T are the bacterial colonies number for the control and test, respectively.

2.6. Checkerboard assay

To determine the performance of nABs in improving the antibacterial effect of antibiotics (amox-clav), the microdilution checkerboard method was used (Tantisuwanno et al., 2021). The assay was performed in 96-well microplates, where a serial dilution of amox-clav was distributed into the wells of the first row to obtain varying concentrations (1/2 MIC, 1/4 MIC, and 1/8 MIC), while nABs were similarly distributed among the first column to obtain the sublethal concentrations (0.12, 0.25, 0.5, and 1 mg/mL for MDR-isolates and 0.06, 0.12, 0.25, and 0.5 mg/mL for standard bacterium). The amox-clav dilutions were started from the second column to the right and nABs were started from the second row downwards. Consequently, each of the wells held a unique combination of nABs and amox-clav concentrations. The wells were inoculated with 10 μL of each test bacteria (0.5 McFarland) to yield the appropriate density of 10^5 CFU/well and incubated at 37 ℃ for 20 h. The OD at 630 nm was recorded. To check the combinatorial antimicrobial activity, the fractional inhibitory concentration indices (FICIs) were calculated according to the following equation:

$$\text{FICI} = \frac{\text{MIC of nABs in combination}}{\text{MIC of nABs alone}} + \frac{\text{MIC of antibiotic in combination}}{\text{MIC of antibiotic alone}}$$

FICI values were interpreted as synergistic (FICI $\leq$ 0.5), no synergism (0.5 $<$ FICI $\leq$ 4), and antagonistic effects (FICI $>$ 4).

2.7. Biofilm inhibition assay

Several assays have been described for biofilm quantification (Peeters et al., 2008; Zhong et al., 2016). The crystal violet assay is often preferred due to its simplicity, reliability, and quick throughput assay. In this study, the antibiofilm activity of nABs was determined against the test MDR-isolates using the crystal violet method (Barani et al., 2021). The turbidity of overnight grown bacterial culture in NB medium was adjusted to 0.5 McFarland. Bacterial suspension (20 μL) was treated with 200 μL of each nABs at different concentrations (0.06, 0.12, 0.25, 0.5, 1, 2, and 4 mg/mL) and incubated at 37 ℃ for 24 h. The microtube containing inoculum without nABs was considered as a control. After incubation time, the culture supernatant was discarded and tubes were washed twice with phosphate-buffered saline (PBS, pH = 7.4) to remove non-adherent cells. The adherent bacterial cells were subjected to 230 μL of 0.1 % w/v crystal violet for 10 min. Afterward, the tubes were washed with PBS to remove the excess crystal violet and dried at room temperature. Eventually, 200 μL of 30 % v/v acetic acid was added to each tube and after 15 min, the absorbance was measured at 630 nm. The percentage of biofilm inhibition was calculated using the following equation:

$$\text{Biofilm Inhibition}\,(\%) = \left(\frac{\text{OD}_{\text{Control}} - \text{OD}_{\text{Sample}}}{\text{OD}_{\text{Control}}}\right) \times 100$$

2.7.1. Biofilm inhibition assay using light microscopy

The inhibition of biofilm formation of the test bacteria in the presence of nABs was further studied using light microscopy. The MDR-isolates were cultured in the absence and presence of nABs at the final concentration of 2 mg/mL on sterile glass coverslips (1 × 1 cm^{-2}) in a tissue culture plate. The plates were incubated at 37 ℃ for 24 h. After the incubation time, the glass coverslips were removed from wells and washed three times with sterile PBS to remove non-attached cells. The glass surfaces were stained with 0.1 % crystal violet solution for 20 min. The excess amount of stain was removed by gentle washing and the coverslips were air-dried at room temperature. The biofilms were visualized under a light microscope and images were captured using 40 × magnification. The thickness of biofilm was measured by light microscopy technique (Bakke and Olsson, 1986).

2.8. Antioxidant assay

The antioxidant activity of MNPs was evaluated using 2,2-diphenyl-1-picrylhydrazyl (DPPH) color change assay, which is known as the free radical scavenging assay. Freshly prepared DPPH in methanol (100 μL, 0.04 % w/v) was added to each microplate well containing 100 μL of different MNPs concentrations (0.06, 0.12, 0.25, 0.5, 1, 2, 4, and 8 mg/mL). After incubation for 30 min at room temperature in the dark, the absorbance of stable DPPH was recorded at 492 nm. The wells containing DPPH + methanol and different concentrations of MNPs + methanol were considered as a control and blank, respectively. Ascorbic acid was used as a reference standard. Free radical scavenging activity was expressed as the percentage of inhibition, which was estimated using the following equation:

$$\text{DPPH Radical Scavenging Activity } (\%) = [\frac{A_C - (A_T - A_B)}{A_C}] \times 100$$

where A_T is the absorbance of test wells, A_B is the absorbance of blank wells, and A_C is the absorbance of control well.

2.9. Determination of cell membrane integrity

The integrity of bacterial cell membranes in the presence of nABs was monitored using two methods: extracellular lactate dehydrogenase (LDH) and protein leakage assays.

2.10. Lactate dehydrogenase assay

Lactate Dehydrogenase (LDH) assay was performed to quantitatively determine the extent of bacterial cell damage. This was estimated by measuring the LDH activity level in the oxidation of reduced nicotinamide adenine dinucleotide (NADH) using a commercial LDH assay kit (Parsazmoon, Iran). Bacterial cells (10^5 CFU/mL) were treated with different concentrations of nABs (0.25, 0.5, and 1 mg/mL) and incubated at 37 ℃ for 6 h. After incubation, the mixture was centrifuged and the supernatant was added to the LDH reaction solution containing NADH and pyruvate. Absorbance was recorded for 1 to 5 min, and the relative change in the absorbance per min was calculated at 340 nm using Eppendorf BioPhotometer plus (Eppendorf, Germany). Bacterial cells without nABs were also considered as a control.

2.11. Protein leakage assay

To investigate bacterial cell wall disruption during treatment with nABs, protein concentration in the supernatant was quantified using the Bradford assay. Bacterial cells were inoculated in NB medium to a final density of 10^5 CFU/mL. The bacterial cells were treated with different concentrations of nABs (0.25, 0.5, and 1 mg/mL) and incubated at 37 ℃. After incubation for 6 h, the samples were centrifuged and the supernatant was collected. To quantify the protein concentration, 100 μL of the supernatant was treated with 100 μL of Bradford reagent. The mixture was incubated for 30 min in the dark at room temperature. The absorbance was measured at 630 nm. Bovine serum albumin (BSA) was used as a standard protein. The total protein concentration was determined by extrapolating the standard curve.

2.12. Statistical analysis

The experiments were repeated at least three times, and the results were represented as mean ± standard deviation (SD). Statistical analysis was carried out using GraphPad Prism software, with a probability of $p < 0.05$. One-way ANOVA was used to compare the differences among group means with the pooled standard deviations of the groups. Also, nonlinear regression was used to determine the MIC_{50} and EC_{50} values.

3. Results and discussions

Nanoantibiotics have been widely studied for their potential to combat pathogenic microorganisms and improve antibiotic-dependent therapies. Specifically, biosynthesized nABs have been found to have significant antibacterial and antibiofilm activities. The aim of this study was to evaluate the effect of two biosynthesized nABs (TiO_2 NPs and ZnO NPs) in improving the antibacterial activity of amox-clav antibiotics against two MDR-pathogens. The study also investigated the antibiofilm and antioxidant activities of the nABs.

3.1. Nanoparticles biosynthesis

The cell-free extract of *V. harveyi* VLC was used to synthesize TiO_2 NPs and ZnO NPs. The process involved adding a determined amount of precursor salt solution to the bacterial cell-free extract and incubating the mixture in a water bath at 100 ℃ for 1 h. At the beginning of the incubation time, a white precipitate was observed at the bottom of the flasks, confirming the formation of MNPs. The appearance of white precipitate during the formation of TiO_2 NPs and ZnO NPs was also reported in previous studies (Masoudi et al., 2018; Barani et al., 2021).

3.2. Nanoantibiotics characterization

The optical and geometrical properties of the prepared MNPs alone and in combination with amox-clav were investigated using UV–Visible spectroscopy in the range of 200–800 nm (Fig. 1a and b). Results showed a unique sharp absorption peak at 250 and 260 nm for TiO_2 NPs and ZnO NPs, respectively which is consistent with previous reports (Masoudi et al., 2018; Barani et al., 2021). These results indicate that both prepared MNPs have the ability to absorb ultraviolet radiation. Furthermore, considerable sharp absorption of TiO_2 NPs and ZnO NPs implies that the MNPs are small in size, spherical, and monodispersed (Mehdizadeh et al., 2022). The UV–Visible absorption spectra of TiO_2 NPs/amox-clav and ZnO NPs/amox-clav demonstrated an additional strong absorption peak at around 220 nm, corresponded to the maximum absorption of amox-clav (Cercel et al., 2023). The absorption edges of TiO_2 NPs, ZnO NPs, TiO_2 NPs/amox-clav, and ZnO NPs/amox-clav were determined at 390, 354, 289, and 290 nm, respectively. The band gap energy (E_g) of the samples was calculated both using absorption edge (Eq. (1) and by plotting the graph of $h\nu$ versus $(\alpha h\nu)^m$ followed by extrapolating the straight line to $(\alpha h\nu)^m = 0$ based on Tauc/David–Mott model (Eq. (2).

$$E_g = \frac{hc}{\lambda} \tag{1}$$

$$(\alpha h\nu)^m = A(h\nu - E_g) \tag{2}$$

where h is Planck constant (4.14×10^{-15} eV.s), c is the speed of light ($3 \times 10^8 m.s^{-1}$), λ is wavelength (m), A is a proportionality constant, ν is the frequency of light, and α is the absorption coefficient. The value of the exponent m denotes the nature of the sample transition so that it is 2 or 1/2 for allowed direct and indirect transitions, respectively. Table 1 shows the band gap energies calculated using both methods, with similar results obtained from the two methods. The band gap energy of TiO_2 NPs was narrowed from 3.23 eV for standard anatase to 3.18 eV, while it was widened from 3.37 eV to 3.50 eV for ZnO NPs. The decreased energy band gap of TiO_2 NPs may be due to the possible presence of trap states within the conduction and valence bands. Biologically synthesized TiO_2 NPs with the lower band gap energy of 2.80 eV and 2.52 eV were synthesized using *Bacillus subtilis* and *Wrightia tinctoria* leaf extract, respectively (Muthuvel et al., 2021; Mansoor et al., 2022). It was reported that biologically synthesized TiO_2 NPs have lower band gap energy than bulk pure TiO_2 NPs due to the quantum-confinement effects, which could have biological significance (Verma et al., 2022). The increased energy band gaps of biogenic ZnO NPs at

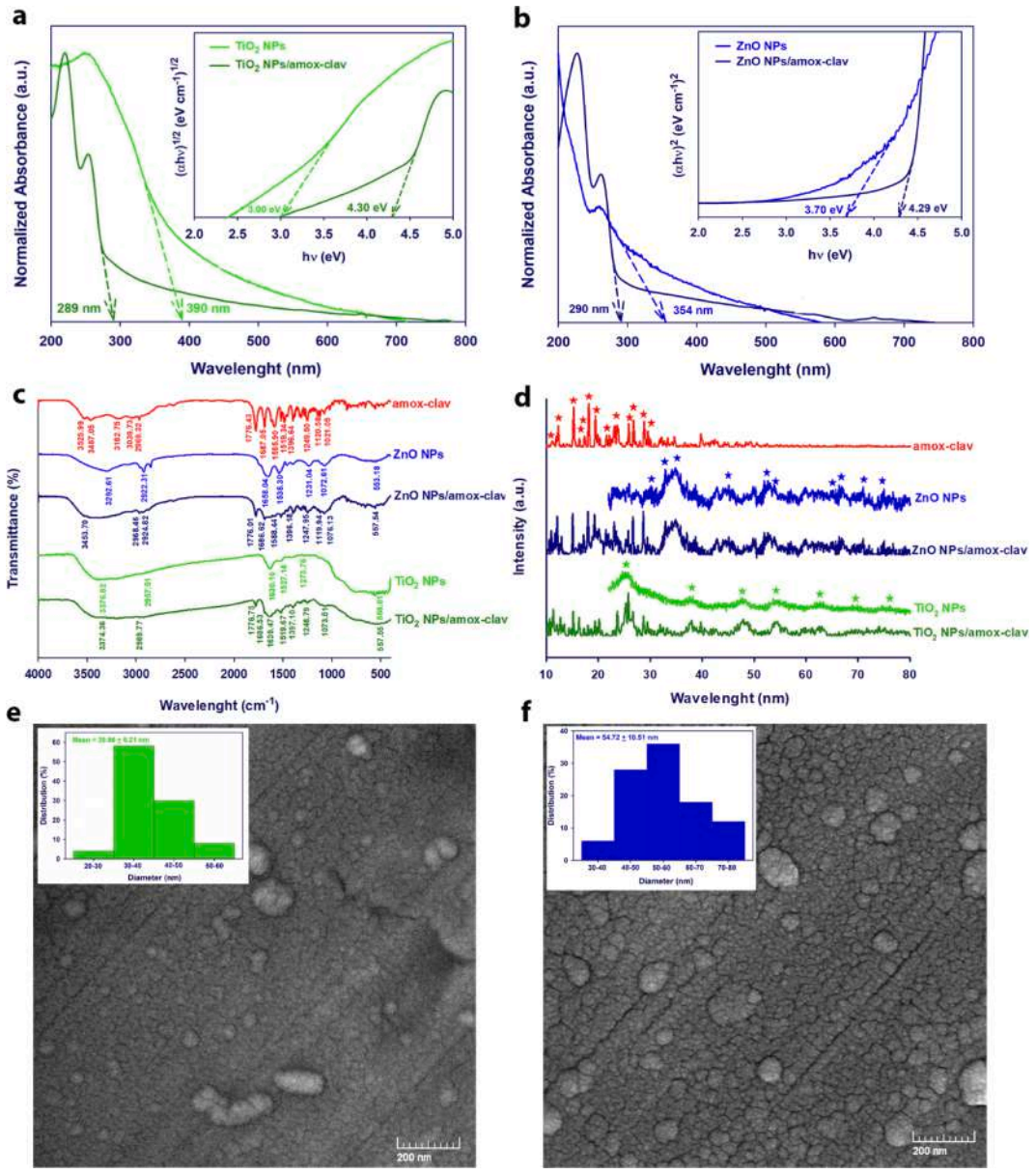

Fig. 1. Characterization of the samples. The UV–Visible absorption spectra (a and b), FTIR spectra (c), and XRD patterns (d) of TiO_2 NPs, ZnO NPs, TiO_2 NPs/amox-clav, and ZnO NPs/amox-clav. The insect pictures show the energy band gap values corresponding to Tauc plots. The FESEM images (e and f) of TiO_2 NPs and ZnO NPs. The insect pictures show the particle size distribution (PSD) of the samples.

Table 1
The band gap energies (E_g) calculated using absorption edge and Tauc/David–Mott model for TiO_2 NPs, ZnO NPs, TiO_2 NPs/amox-clav, and ZnO NPs/amox-clav.

Sample	E_g (eV)	
	Absorption edge	Tauc model
TiO_2 NPs	3.18	3.00
ZnO NPs	3.50	3.70
TiO_2 NPs/amox-clav	4.30	4.30
ZnO NPs/amox-clav	4.29	4.29

3.54, 3.51, and 3.63 eV were reported by Sharma et al. (Sharma et al., 2022b), Maalmarugan et al. (Maalmarugan et al., 2022), and Singh et al. (Singh et al., 2019), respectively. It was mentioned that the increased band gap energy of ZnO NPs results from a blue shift in the maximum absorption due to the decreased particle size. The band gap energy value of TiO_2 NPs/amox-clav and ZnO NPs/amox-clav was found to be higher than that of pure TiO_2 NPs and ZnO NPs. It was determined 4.30 and 4.29 eV for TiO_2 NPs/amox-clav and ZnO NPs/amox-clav, respectively. This indicated that the addition of amox-clav to the MNPs resulted in an increase in band gap energy. This phenomenon is in line with the Moss-Burstein theory, which suggests that the donor electrons occupy states at the bottom of the conduction band, requiring extra energy for the valence electrons of doped MNPs to transition to higher states than that of pure MNPs (Mohammadi et al., 2012).

The FTIR spectra of the samples were investigated in the range of 400–4000 cm^{-1} to identify the bacterial bioactive molecules present on the surface of the samples that contributed to their bioreduction and stability. Fig. 1c shows a significant resemblance between the FTIR absorption spectra of TiO_2 NPs and ZnO NPs. The absorption bands at around 3300, 2930, 1630, 1530, and 1230 cm^{-1} were observed for both samples. The intensive broad absorption band at 3300 cm^{-1} is assigned to O –H stretching and the presence of carboxylic acid (Unger and Coclite, 2022). The peaks at 2930 and 1530 cm^{-1} described C –H and N

−H bending of amide II (Sharmila et al., 2019). The band at 1230 cm^{-1} is attributed to C −N stretching of amide III, while the band at 1630 cm^{-1} represents C = O stretching of amide I (Tripathi et al., 2022). The broad bands at 558.51 and 553.18 cm^{-1} attributed to Ti −O and Zn −O stretching modes and confirmed the synthesis of TiO_2 NPs and ZnO NPs, respectively. It was reported that the bands between 400 and 650 cm^{-1} attributed to the metal–oxygen bond bending (Chinnathambi et al., 2023). The obtained data led to the conclusion that bioactive molecules including hydroxyl, amine, and carboxyl of bacterial proteins were responsible for the reduction and synthesis of TiO_2 NPs and ZnO NPs. In previous studies, it was recognized that proteins as capping agents are responsible for the stability and bioreduction of MNPs (Masoudi et al., 2018; Barani et al., 2021). Similarly, other studies have reported that secreted bacterial proteins are responsible for the stabilization of TiO_2 NPs and ZnO NPs (Mansoor et al., 2022). The FTIR absorption spectra of amox-clav demonstrated bands in the region between 3500 and 3200 cm^{-1} associated to O −H stretching of the phenol and carboxylic group (Min et al., 2020) and N −H stretching of the primary amine and secondary amide. The bands around 3000 cm^{-1} are attributed to the symmetrical and asymmetrical stretching of C −H of benzene ring (Foschi et al., 2022). The bands at around 1766 and 1687 cm^{-1} are assigned to C = O stretching of the β-lactam ring and the secondary amide, respectively (Hadizadeh and Toraji, 2019). The bands in the region between 1500 and 1300 cm^{-1} are associated to C = C stretching of the aromatic ring and N −H bending of the secondary amide, whereas the bands at around 1250 cm^{-1} is provided by the C −N stretching of the primary amine (Müller et al., 2011). Furthermore, the bands at around 1000 cm^{-1} are attributed to the stretching vibration of C −O bending (Songsurang et al., 2011). The FTIR spectra of TiO_2 NPs/amox-clav and ZnO NPs/amox-clav demonstrated the characteristic bands related to the amox-clav and MNPs, providing evidence of the combination of amox-clav and MNPs.

The XRD was used to determine the phase purity and crystal structure of the prepared TiO_2 NPs and ZnO NPs. The XRD patterns of TiO_2 NPs, ZnO NPs, amox-clav, TiO_2 NPs/amox-clav, and ZnO NPs/amox-clav are shown in Fig. 1d. The XRD pattern of TiO_2 NPs showed diffraction peaks assigned to the lattice planes of (101), (004), (200), (211), (204), (220), and (215), which were consistent with the standard TiO_2 NPs diffraction reported from Joint Committee on Powder Diffraction Standards file (JCPDS No. 01–071-1166) and confirmed the formation of the high purity of anatase structure TiO_2 NPs. For ZnO NPs, the peaks corresponded to the lattice planes of (100), (002), (101), (102), (110), (200), (112), (004), and (202), which were consistent with JCPDS No 96–230-0113 and confirmed the formation of ZnO NPs with hexagonal structure. The obtained results were in good agreement with previous reports (Masoudi et al., 2018; Barani et al., 2021). The XRD pattern of amox-clav alone and in combination with MNPs was taken for the 2θ range of 10 to 80°. The XRD pattern of amox-clav demonstrated strong and sharp peaks at 2θ of 11.12, 11.92, 12.28, 15.23, 16.36, 17.32, 18.15, 19.43, 22.57, 23.13, 23.62, 25.85, 26.79, and 28.81°, attributed to crystalline structure of amoxicillin trihydrate and potassium clavulanate (Obaidat et al., 2022). The XRD patterns of TiO_2 NPs/amox-clav and ZnO NPs/amox-clav showed the related peaks for both amox-clav and MNPs, confirming the combination of MNPs with amox-clav.

The shape and size of TiO_2 NPs and ZnO NPs were examined using FESEM. The results (Fig. 1e and f) demonstrated spherical-shape TiO_2 NPs and ZnO NPs with average particle size of 39.86 ± 6.21 and 54.72 ± 10.51 nm, respectively. The hydrodynamic size of the biogenic samples was determined using DLS and was found to be 38.65 nm (PDI = 0.22) and 57.87 nm (PDI = 0.51) for TiO_2 NPs and ZnO NPs, respectively. Zeta potential was performed to determine the stability of the samples in bacterial culture medium (NB medium). The zeta potential values greater than + 30 mV or less than −30 mV typically have a high degree of stability. The average zeta potential value of –22.33 ± 10.11 mV for TiO_2 NPs and −25.66 ± 11.57 mV for ZnO NPs indicated that both samples were stable in NB medium, but ZnO NPs seemed to be more stable. Moreover, based on zeta potential values, it was found that both biologically synthesized samples are monodispersed materials. Comparably, the zeta values of −27.41, −25.1, and −28.2 mV with the average particle size between 10 and 110 nm were determined for biogenic ZnO NPs synthesized by *Pseudochrobactrum* sp. (Siddique et al., 2021), Stevia leaves (Khatami et al., 2018), and *Gracilaria edulis* extract (R et al., 2019), respectively. TiO_2 NPs of present study showed similar characteristics to previous studies (Balaraman et al., 2022; Dessai et al., 2022).

The role of bacterial proteins in the biosynthesis of MNPs was evaluated using the Bradford protein assay. Fig. 2a shows the amount of protein measured by extrapolating the BSA standard curve. The results demonstrated that as the concentration of MNPs increased, the protein concentration also increased. The protein concentration was augmented by 4- and 2-fold when the concentration of TiO_2 NPs and ZnO NPs varied from 0.25 to 2 mg/mL, respectively. These results were in accordance with the FTIR analysis confirming the key role of bacterial proteins in the biosynthesis and stabilization of TiO_2 NPs and ZnO NPs. Moreover, according to the same results, TiO_2 NPs had a higher protein content than ZnO NPs. This principle can be related to zeta potential results, in which the low negative zeta potential of TiO_2 NPs could be due to the presence of more amino groups of proteins on the MNPs surface. The fluorescence emission spectra of the MNPs samples are shown in Fig. 2b. A broad emission spectrum with the maximum peak at around 530 and 520 nm was obtained for TiO_2 NPs and ZnO NPs, respectively. The fluorescent properties of TiO_2 NPs and ZnO NPs could be attributed to the oxygen-vacancy-related surface defects and quantum confinement effect of MNPs (Das et al., 2018; Zhou et al., 2023). Moreover, bacterial flavoprotein, i.e. flavin mononucleotide (FMN) as one of the major proteins in the stabilization and biosynthesis of MNPs using bioluminescence bacteria, has an excitation and emission wavelength at 450 and 530 nm, respectively (Masoudi et al., 2018). FMN plays a key role in the formation of luminescent nanoparticles.

3.3. Antibacterial activity

The antibacterial activity of nABs was determined against MDR-isolates, including A. *baumannii* 80 and *E. coli* 27G, and standard bacterium including *E. coli* ATCC 25922. The antibiotic-resistant profile of the test bacteria was determined and compared with the standard bacterium. MIC, MBC, and CF assays were performed to assess the effectiveness of the samples. The synergistic antibacterial activity of the samples with amox-clav antibiotics was determined using checkerboard assay.

3.3.1. Antibiotic susceptibility test

The Kirby-Bauer disc diffusion technique was used to determine the antibiotic-resistance profile of the bacteria, and the results were compared with the standard *E. coli* ATCC 25922 as a control (Table 2 and Fig. 3). *A. baumannii* 80 and *E. coli* 27G were both 100 % resistant to seven antibiotics out of 17 tested including, NA, PIP, AMC, CN, AM, CZ, and AMX. However, while *A. baumannii* 80 was 100 % resistance to all 17 antibiotics tested, *E. coli* 27G was sensitive to three antibiotics, AN, GM, and LEV, and resistant to the remaining 14 antibiotics. Similar outcomes were found in other studies (Dar et al., 2022).

3.3.2. Determination of MIC and MBC

The antibacterial activities of biogenic TiO_2 NPs, ZnO NPs, and amox-clav were evaluated against *E. coli* ATCC 25922 and MDR-isolates, *A. baumannii* 80 and *E. coli* 27G clinical isolates, using the micro-broth dilution method. The MIC and MBC values of the samples are given in Table 3. The obtained MIC values (MBC values) for amox-clav, TiO_2 NPs, and ZnO NPs were 8 (8), 2 (>8), and 4 (8) mg/mL against *A. baumannii* 80 and 1 (2), 2 (>8), and 4 (8) mg/mL against *E. coli* 27G, respectively. The MIC (MBC) values of amox-clav, TiO_2 NPs, and ZnO NPs were also determined 0.06 (0.06), 1 (>8), and 0.5 (4) mg/mL against *E. coli* ATCC

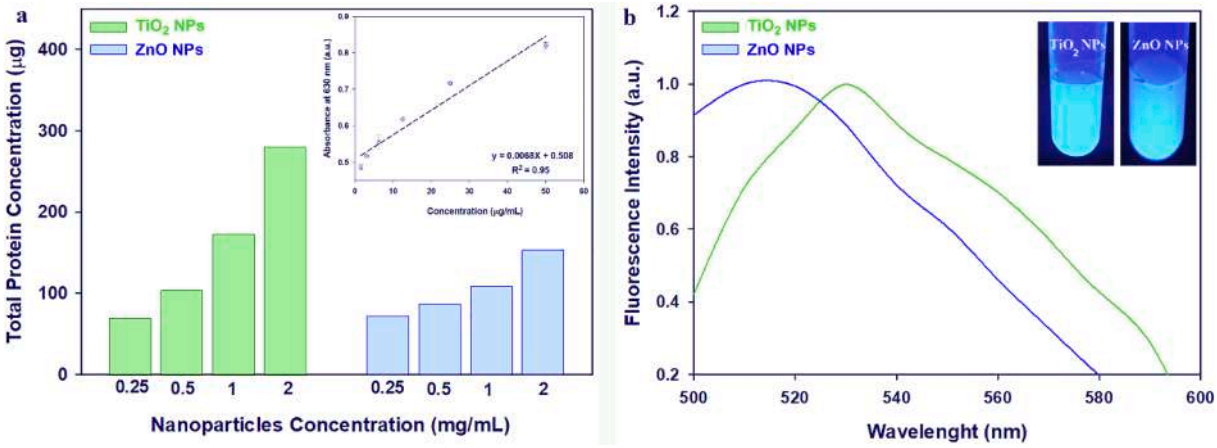

Fig. 2. Protein Assay. The amount of protein on the surface of TiO_2 NPs and ZnO NPs at different concentrations was calculated using extrapolating the standard curve of BSA (insect picture) by Bradford assay (a). The fluorescence emission spectra of TiO_2 NPs and ZnO NPs at 450 nm excitation wavelength (b). The insect pictures show the fluorescent property of the samples under a UV lamp at 365 nm.

Table 2
Antibiotic-resistance profile of *A. baumannii* 80, *E. coli* 27G, and *E. coli* ATCC 25922.

Antibiotics (µg/Disk)	Inhibition Zone Diameter (mm)		
	A. baumannii 80	*E. coli* 27G	*E. coli* ATCC 25922
AN (30 µg)	0 (R)	20 (S)	22 (S)
CP (5 µg)	0 (R)	15 (R)	26 (S)
GM (10 µg)	0 (R)	20 (S)	22 (S)
NA (30 µg)	0 (R)	0 (R)	0 (R)
SXT (1.25/23.75 µg)	0 (R)	0 (R)	20 (S)
LEV (5 µg)	9 (R)	16 (S)	26 (S)
CRO (30 µg)	0 (R)	0 (R)	25 (I)
PIP (100 µg)	0 (R)	0 (R)	8 (R)
AMC (30 µg)	0 (R)	0 (R)	12 (R)
IPM (10 µg)	0 (R)	8 (R)	22 (S)
FOX (30 µg)	0 (R)	0 (R)	16 (I)
CN (30 µg)	0 (R)	0 (R)	14 (R)
CZ (30 µg)	0 (R)	0 (R)	0 (R)
CB (100 µg)	0 (R)	0 (R)	26 (S)
AM (10 µg)	0 (R)	0 (R)	10 (R)
AMX (25 µg)	0 (R)	0 (R)	0 (R)
TIC (75 µg)	0 (R)	0 (R)	28 (S)

AN: Amikacin; CP: Ciprofloxacin; GM: Gentamicin; NA: Nalidixic acid; SXT: Trimethoprim sulfamethoxazole; LEV: Levofloxacin; CRO: Ceftriaxone; PIP: Piperacillin; AMC: Amoxicillin-clavulanic acid; IPM: Imipenem; FOX: Cefoxitin; CN: Cephalexin; CZ: Cefazolin; CB: Carbenicillin; AM: Ampicillin; AMX: Amoxicillin; TIC: Ticarcillin. R: Resistant; S: Sensitive; I: Intermediate.

25922 as an indicator bacterium.

A dose-dependent antibacterial activity was observed for all samples in which the viability of strains decreased with increasing the sample concentrations (Fig. 4a, b, and c). The MIC_{50} values of amox-clav, TiO_2 NPs, and ZnO NPs, representing the concentration at which 50 % of the isolates in a test population are inhibited, were found to be 1.93, 0.17, and 0.21 mg/mL against *A. baumannii* 80, 0.24, 0.15, and 0.17 mg/mL against *E. coli* 27G, and 0.01, 0.042, and 0.058 mg/mL against *E. coli* ATCC 25922, respectively. The results showed a considerable higher antimicrobial effect of biogenic nanoparticles (nABs) compared to amox-clav against *A. baumannii* 80, while no significant difference was observed against *E. coli* 27G. This suggests that *A. baumannii* 80 is more resistant to antibiotics than *E. coli* 27G, which was later confirmed by the antibiotic susceptibility test. Overall, both biogenic TiO_2 NPs and ZnO NPs were found to be considerably effective nABs against MDR-isolates. In terms of bacteriostatic and bactericidal activity, TiO_2 NPs exhibited better bacteriostatic activity than ZnO NPs against both MDR-isolates based on MIC_{50} values. This could be attributed to the lower negative zeta potential of TiO_2 NPs, which facilitates their interaction with the negatively charged elements of bacterial cell wall. However, according to MBC results, higher bactericidal activity was observed for ZnO NPs compared to TiO_2 NPs against all tested bacteria. This is supported by the studies reporting higher antibacterial efficiency of ZnO NPs compared to TiO_2 NPs against various bacteria, including *P. fluorescence, L. Monocytogenes,* MDR-*A. baumannii*, and *E. coli* (Kareem et al., 2019; Yuan et al., 2021).

The size of nanoparticles plays a crucial role in their bactericidal activity. Small nanoparticles can penetrate bacterial cell walls easily, but they are expelled out through multidrug efflux pumps, contributing to the antibiotic resistance. On the other hand, large nanoparticles can create larger holes in the cell wall, causing higher bactericidal activity (Nieto-Maldonado et al., 2022). These could be related to the higher bactericidal activity of large ZnO NPs (57.87 nm) compared with small TiO_2 NPs (38.65 nm).

The antibacterial activity of TiO_2 NPs and ZnO NPs is mainly due to the generation of reactive oxygen species (ROS) and release of antimicrobial ions (Hamk et al., 2023; Kumari et al., 2023). The production of ROS, such as the superoxide radical (O^{-2}), the hydroxyl radical ($^{\circ}OH$), hydrogen peroxide (H_2O_2), and singlet oxygen ($^1O_2$), on the surface of TiO_2 NPs and ZnO NPs can cause serious damage to nucleic acids, lipids, and proteins, which ultimately kills bacteria. This is the main mechanism behind the antibacterial activity of TiO_2 NPs. On the other hand, the antibacterial activity of ZnO NPs is mainly due to the release of Zn^{+2} ions from the nanoparticles in aqueous suspension, which have multiple inhibitory effects on crucial metabolic processes in bacterial cells (Hutchings et al., 2021).

Moreover, the incorporation of TiO_2 NPs and ZnO NPs causes the transformation of electrons from the conduction band of ZnO NPs to the conduction band of TiO_2 NPs and similarly, the holes from the valence band of TiO_2 NPs transferred to the valence band of ZnO NPs. This process increases the availability of electron and hole pairs at the surface of nanocomposites which consequently enhances ROS generation in aqueous media (Samal et al., 2024).

The bacterial cell viability was assessed by enumerating the colony forming units (CFU/mL) when MDR-bacterial strains were exposed to different concentrations of TiO_2 NPs and ZnO NPs (1, 2, 4, and 8 mg/mL). In this assay, the bacterial cells were grown in the absence and presence of nABs for 12 h. Then, CFUs counts were performed to determine the number of viable cells and the rate of bactericidal effect (Fig. 5 and Table 4). The results showed that the CFU of *A. baumannii* 80 and *E. coli* 27G significantly decreased with increasing concentrations of nABs. Both nABs were more effective against *E. coli* 27G than *A. baumannii* 80. Overall, ZnO NPs exhibited the superior bactericidal

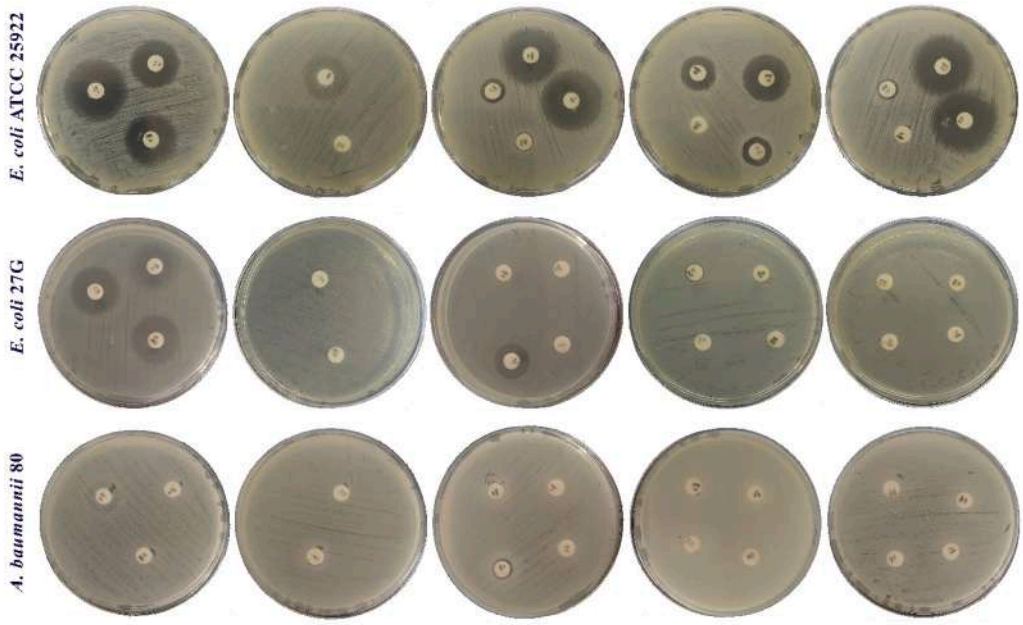

Fig. 3. Antibiotic susceptibility testing plates of *A. baumannii* 80, *E. coli* 27G, and *E. coli* ATCC 25922 strains.

Table 3
Minimum inhibitory concentration (MIC) and minimum bactericidal concentration (MBC) values of the amox-clav, TiO_2 NPs, and ZnO NPs against MDR-isolates including *A. baumannii* 80 and *E. coli* 27G as well as standard *E. coli* ATCC 25922.

Bacteria Tested	amox-clav		TiO_2 NPs		ZnO NPs	
	MIC	MBC	MIC	MBC	MIC	MBC
***A. baumannii* 80**	8	8	2	>8	4	8
***E. coli* 27G**	1	2	2	>8	4	8
***E. coli* ATCC 25922**	0.06	0.06	1	>8	0.5	4

activity compared with TiO_2 NPs. These findings are consistent with the MIC and MBC results and are comparable with the results of previous studies.

3.4. Checkerboard assay

In order to evaluate the synergistic effect of nABs in combination with antibiotics (amox-clav), sublethal concentrations of nABs (0.12, 0.25, 0.5, and 1 mg/mL for MDR- isolates and 0.06, 0.12, 0.25, and 0.5 mg/mL for standard bacterium) and amox-clav (MIC/2, MIC/4, and MIC/8) were used in a checkerboard assay. The results of fractional inhibitory concentration index (FICI) indicated synergistic antibacterial effects of nABs and antibiotics, with FICIs ≤ 0.5 (Table 5). The MIC value of amox-clav was significantly reduced by 8-fold when combined with nABs against *A. baumannii* 80, and *E. coli* 27G. For *A. baumannii* 80, the MIC values decreased from 8 to 1 mg/mL, and for *E. coli* 27G, it decreased from 1 to 0.12 mg/mL. These results demonstrated that the combination of antibiotics with TiO_2 NPs and ZnO NPs could be more effective against MDR-bacterial strains. Moreover, the MIC value of amox-clav against *E. coli* ATCC 25922 was reduced by 6- and 8.5-fold in combination with TiO_2 NPs and ZnO NPs, respectively.

The search results provided some relevant information on the synergistic effects of TiO_2 NPs and ZnO NPs with different antibiotics against pathogens (Thakral et al., 2021; Ribeiro et al., 2022). For example, a study reported the increased antibacterial activity of amox-clav in the presence of ZnO NPs against MRSA strains (Sharif et al., 2021). The results showed positive synergistic effects of ZnO NPs on amox-clav, leading to enhanced killing of amox-clav resistant MRSA isolates. It is believed that the combination of antibiotics with MNPs increases the uptake of antibiotics due to the disruption of bacterial cells caused by the MNPs (Nallal et al., 2022).

3.5. Antibiofilm activity

The inhibitory effect of biosynthesized nABs (TiO_2 NPs and ZnO NPs) on biofilm formation was investigated using the crystal violet method. The MDR-isolates, *A. baumannii* 80 and *E. coli* 27G, were treated with different concentrations of nABs (0.06, 0.12, 0.25, 0.5, 1, 2, and 4 mg/mL) for 24 h. The results showed a significant reduction in biofilm formation in a dose-dependent manner (Fig. 6). Specifically, the biogenic ZnO NPs inhibited 100 % of *E. coli* 27G biofilm formation at a concentration of 2 mg/mL, while the maximum inhibition of *E. coli* 27G biofilm formation (~75 %) occurred at 4 mg/mL of TiO_2 NPs. For *A. baumannii* 80, biofilm formation was inhibited by about 45 % and 50 % at a high concentration of TiO_2 NPs and ZnO NPs (4 mg/mL), respectively. The conclusion that ZnO NPs have higher antibiofilm activity than TiO_2 NPs on both MDR-isolates ($p < 0.0001$) is likely due to the higher bactericidal activity of ZnO NPs. When bacteria were treated with ZnO NPs, the decreased cell viability resulted in the reduction of biofilm production. Also, it is found that *E. coli* 27G biofilm formation was effectively inhibited by both biogenic TiO_2 NPs and ZnO NPs.

Previous studies have investigated the antibiofilm activity of TiO_2 NPs and ZnO NPs against certain bacteria (Achudhan et al., 2020; Doğan and Kocabaş, 2020; Altaf et al., 2021; Barani et al., 2021) but only a few reports have been published related to MDR-strains. For example, Baig et al. (Baig et al., 2020) found inhibition percentage of 37.5 % and 22.3 % in the biofilm formation of MRSA and *Pseudomonas aeruginosa*, respectively at 2.5 mg/mL of TiO_2 NPs. These results are comparable to the findings in this study, where 38 % and 17 % inhibition of biofilm formation were obtained for *A. baumannii* 80 and *E. coli* 27G, respectively at a concentration of 2 mg/mL of TiO_2 NPs. It is assumed that TiO_2 NPs significantly downregulates the efflux pump genes (*mexY*, *mexB*, *mexA*) and quorum sensing-regulated genes (*iasR*, *iasI*, *rhIR*, *pqsA*, *pqsR*) that control biofilm formation in MDR-*Pseudomonas aeruginosa* isolates (Ahmed and Mohammed, 2020). Jasim et al. (Jasim et al., 2020) found that the highest inhibition in biofilm formation (73.95 %) occurred at 10 mg/mL of ZnO NPs for vancomycin-resistant *Staphylococcus aureus* (VRSA) strains, while the ZnO NPs biosynthesized in this study showed

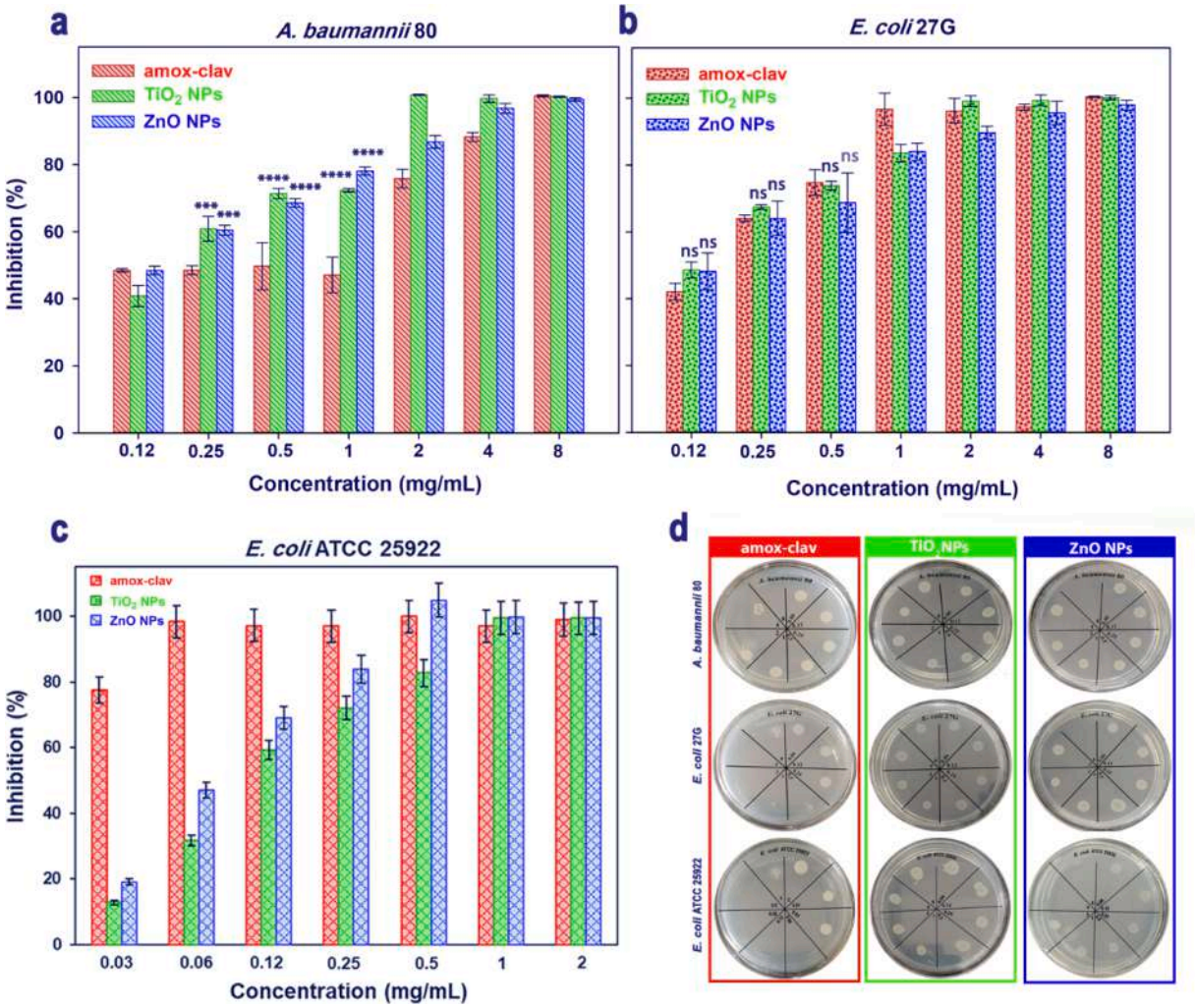

Fig. 4. Antibacterial activity of the antibiotic amox-clav and nABs. Growth inhibition percentage of *A. baumannii* 80 (a), *E. coli* 27G (b), and *E. coli* ATCC 25922 (c) at different concentrations of amox-clav, TiO_2 NPs, and ZnO NPs. The minimum bactericidal concentration (MBC) of the samples against tested bacteria (d).

100 % antibiofilm activity at a lower concentration (4 mg/mL) against *E. coli* 27G isolate. According to previous studies, the formation of the reactive oxygen species (ROS) can be considered one of the main mechanisms for the high and effective antibiofilm activity of TiO_2 NPs and ZnO NPs (Alavi et al., 2019b).

The effect of nABs on the inhibition of *A. baumannii* 80 and *E. coli* 27G biofilm formation was studied on glass coverslips surfaces, followed by light microscopy observations. Fig. 7 shows the biofilm formation of the test bacteria after 24 h of incubation in the absence and presence of 2 mg/mL of TiO_2 NPs and ZnO NPs. The results demonstrated that in the control slides, bacteria heavily colonized on the glass surface, forming a thick layer of biofilm of about 30 and 50 μM for *E. coli* 27G and *A. baumannii* 80, respectively. However, in the slides where nABs were added, significant reduction in bacterial colonization and subsequent inhibition of bacterial biofilm formation were observed.

3.6. Antioxidant activity

The antioxidant activity of the prepared nABs was evaluated using the scavenging of DPPH radical (Fig. 8). The DPPH radical can interact with antioxidant compounds, receiving either electrons or hydrogen atoms, which then become neutralized, and its color changes from intense purple color to a pale yellow. Both biogenic TiO_2 NPs and ZnO NPs showed DPPH radical scavenging activity in the concentrations of 0.06, 0.12, 0.25, 0.5, 1, 2, 4, and 8 mg/mL, with the maximum activity (~100 %) was observed at the concentration of 8 mg/mL for both nABs. The EC_{50} values were found to be about 1.18 and 0.58 mg/mL for TiO_2 NPs and ZnO NPs, respectively. However, the antioxidant activity of ZnO NPs was significantly higher ($p < 0.05$) than that of TiO_2 NPs at lower concentrations which may be due to the higher electron mobility and generation of electron-hole pairs as well as superior quantum efficiency of biogenic ZnO NPs compared to TiO_2 NPs (Chellapandi et al., 2023; Jagadeeswar et al., 2023; Jandaghian et al., 2023).The antioxidant activity of MNPs also depends on their physicochemical characteristics, especially zeta potential (Eramabadi et al., 2020) in which more negative zeta potential of ZnO NPs (-25.66 mV) specified higher antioxidant activity. Alavi et al. reported higher antioxidant activity of ZnO NPs compared to TiO_2 NPs, which is consistent with the given study (Alavi et al., 2019a). They found the maximum DPPH radical scavenging activities of 25.26 ± 3.28, and 14.22 ± 2.88 % for ZnO NPs and TiO_2 NPs, respectively, which is much lower than the results obtained in the given study.

In general, the results of given study were in accordance with previous studies regarding the antioxidant activity of biogenic ZnO (Sharmila et al., 2019; Gur et al., 2022). However, the antioxidant activity observed in the given study particularly around 70 % for 1 mg/mL, was much higher compared to the chemically synthesized ZnO NPs in preceding studies (Iqbal et al., 2022). This difference in antioxidant activity could be attributed to the presence of remaining biomolecules on the surface of the biogenic nABs, which may act as reducing agents and

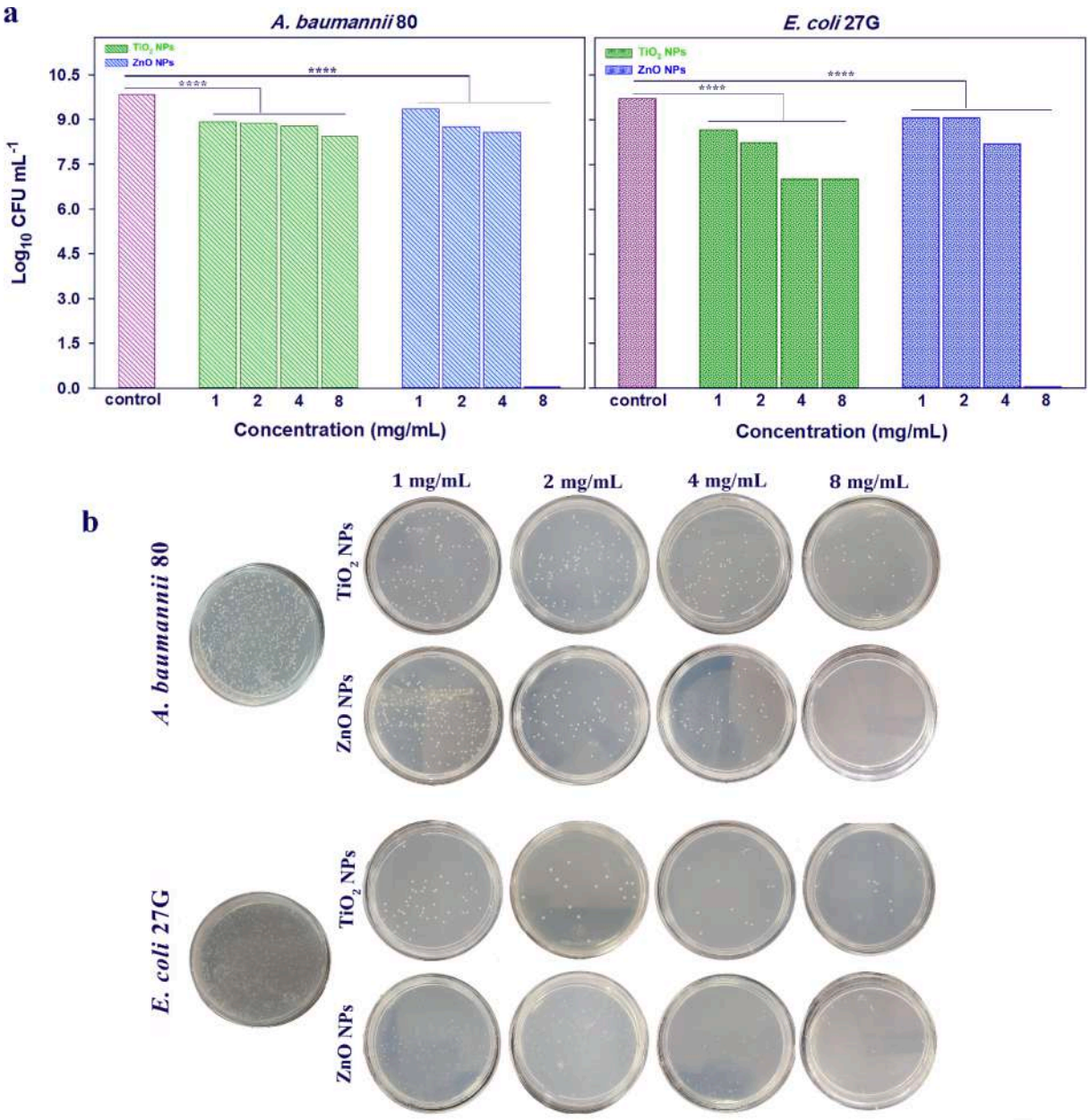

Fig. 5. The bacterial cell viability assay. (a) The effect of different concentrations of nABs on the viable cell number of *A. baumannii* 80 and *E. coli* 27G expressed as the logarithm of the number of colonies grown on plates (CFU/mL). (b) The plates resembling the number of bacterial colonies on agar medium treated with different concentrations of nABs after 12 h incubation. Two plates (first row from left) are considered as controls in which no nABs were added **** < 0.0001.

Table 4
The rate of bactericidal activity (%) of TiO_2 NPs and ZnO NPs against *A. baumannii* 80 and *E. coli* 27G strains.

Bacteria Tested	Bactericidal activity (%)							
	TiO_2 NPs (mg/mL)				ZnO NPs (mg/mL)			
	1	2	4	8	1	2	4	8
***A. Baumannii* 80**	86.55	87.97	90.34	95.72	64.24	89.68	93.98	100
***E. coli* 27G**	89.74	96.12	97.72	97.72	74.03	74.25	96.58	100

enhance the antioxidant properties. Other characteristics of nABs, such as the size of nanoparticle, can also have an effect on antioxidant properties. For example, compared to our nABs, TiO_2 NPs synthesized using *Garcinia mangostana* extract with larger particle size showed less antioxidant activity (34.37 % at 2.5 mg/mL) (Ahn et al., 2022).

3.7. Determination of cell membrane integrity

The study used sublethal concentrations of TiO_2 NPs and ZnO NPs (0.25, 0.5, and 1 mg/mL) to determine the effect of nABs on bacterial cell membrane integrity using LDH and Bradford assays.

Table 5
The MIC and FICI values of antibiotic and the nABs in combination against *A. baumannii* 80, *E. coli* 27G, and *E. coli* ATCC 25922 strains.

Bacteria Tested	TiO_2 NPs		ZnO NPs	
	MICs in combination (amox-clav / MNPs)	FICI	MICs in combination (amox-clav / MNPs)	FICI
***A. baumannii* 80**	(1 / 0.12) mg/mL	0.19	(1 / 0.12) mg/mL	0.16
***E. coli* 27G**	(0.12 / 0.12) mg/mL	0.18	(0.12 / 0.12) mg/mL	0.15
***E. coli* ATCC 25922**	(0.01 / 0.12) mg/mL	0.29	(0.007 / 0.12) mg/mL	0.35

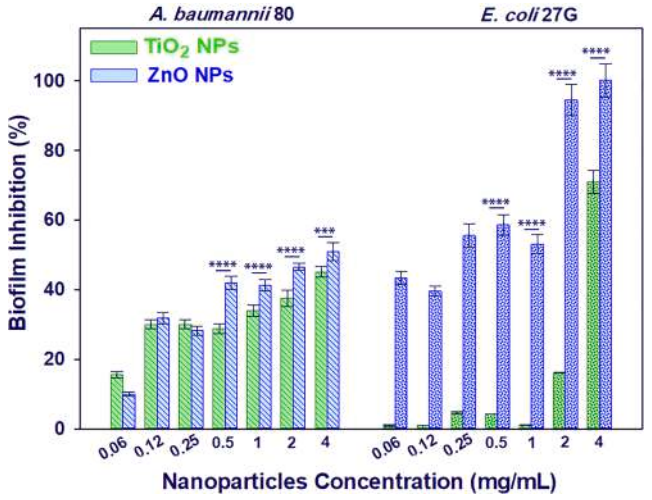

Fig. 6. The biofilm inhibition percentage of bacteria (*A. baumannii* 80 and *E. coli* 27G) at different concentrations of TiO_2 NPs and ZnO NPs. (*** < 0.001; **** < 0.0001).

3.7.1. Lactate dehydrogenase assay

If the bacterial cell membranes are damaged, LDH is released into the culture medium. Therefore, the rate of LDH leakage can be as a criterion for assessing the efficiency of nABs cell cytotoxicity. The LDH assay was performed to determine the degree of membrane damage caused by nABs (TiO_2 NPs and ZnO NPs) in MDR-isolates, *A. baumannii* 80 and *E. coli* 27G, using a commercial kit. The LDH levels were measured in the supernatant of bacteria at the beginning (0 h) and after 6 h incubation with the various concentrations of TiO_2 NPs and ZnO NPs. The results showed that the rate of LDH leakage increased as the dosage of nABs (TiO_2 NPs and ZnO NPs) increased from 0.25 to 1 mg/mL (Fig. 9). In the negative control where no nABs were added, the amount of LDH levels in the supernatant of *A. baumannii* 80 and *E. coli* 27G were found to be 25 and 37 U/L, respectively. However, LDH levels increased when the bacterial cells were treated with different concentrations of TiO_2 NPs and ZnO NPs. Specifically, the amount of LDH level in the supernatant of treated cells with various concentrations of nABs were as follow: 27, 34, and 42 U/L (32, 43, and 53 U/L) for *A. baumannii* 80 and 42, 45, and 48 U/L (43, 48, and 52 U/L) for *E. coli* 27G in the presence of 0.25, 0.5, and 1 mg/mL of TiO_2 NPs (ZnO NPs), respectively. Overall, the degree of LDH leakage was higher in the presence of ZnO NPs, indicating the

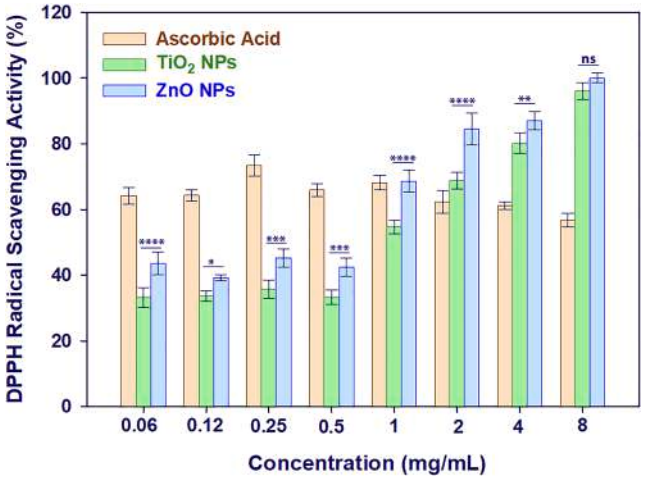

Fig. 8. The antioxidant activity of nABs (TiO_2 NPs and ZnO NPs) at different concentrations. Ascorbic acid was used as positive control. (ns: not significant;* < 0.05; ** < 0.01; *** < 0.001; **** < 0.0001).

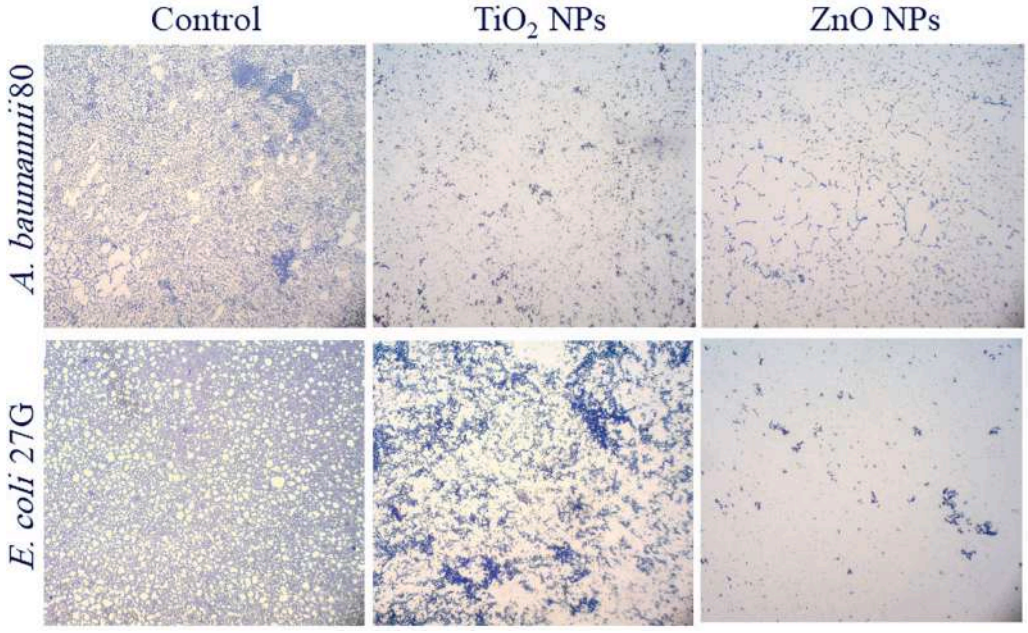

Fig. 7. Light microscopic images of the glass coverslips indicating the effect of 2 mg/mL of TiO_2 NPs and ZnO NPs on the process of bacterial biofilm formation.

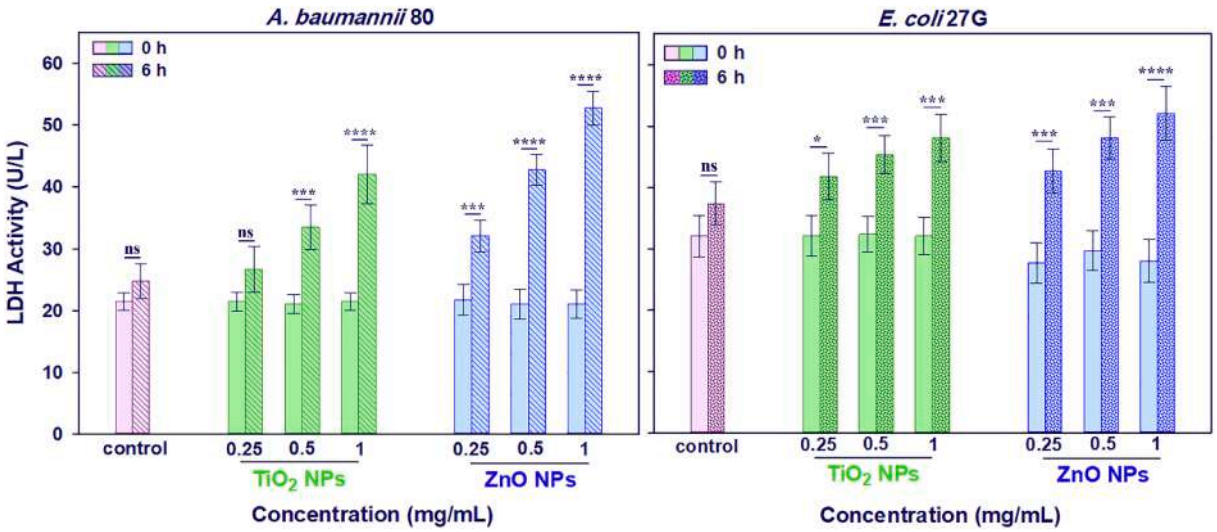

Fig. 9. Lactate dehydrogenase (LDH) activity of *A. baumannii* 80 and *E. coli* 27G after 6 h incubation with different concentrations of TiO_2 NPs and ZnO NPs. (ns: not significant; * < 0.05; *** < 0.001; **** < 0.0001).

higher bacteriolytic activity of ZnO NPs on both MDR-bacterial cells.

Enhanced leakage of LDH from bacteria exposed to nABs signifies more disruption and damage to the bacterial cell envelope, mostly resulted from the generation of free radicals (Velsankar et al., 2020).

3.7.2. Protein leakage assay

The cytotoxicity of the biogenic nABs synthesized in this study was further evaluated by measuring the amount of protein released into the supernatant using Bradford assay (Fig. 10). The results showed that both TiO_2 NPs and ZnO NPs caused an enhanced leakage of intracellular proteins into the extracellular medium in both bacterial strains. The total protein in the supernatant was calculated by extrapolating the BSA standard curve, which was 26 μg/mL for *A. baumannii* 80 and 24 μg/mL for *E. coli* 27G in control samples (without nABs). At concentration of 0.25, 0.5, and 1 mg/mL of TiO_2 NPs and ZnO NPs, the total protein in the supernatant of *A. baumannii* 80 was about 50 (45), 50 (55), 58 (57) μg/mL, respectively. In the supernatant of *E. coli* 27G, the total protein was 47 (45), 48 (46), and 48 (46) μg/mL at the same concentration of TiO_2 NPs (ZnO NPs). These results indicated a significant increase in the protein levels of the bacterial cells supernatant treated with nABs ($p < 0.0001$). After 6 h incubation of bacteria with a high concentration of nABs, the amount of released protein in the supernatant of both bacterial strains was increased about 2-fold. These findings are consistent with previous studies that have shown the disruptive effect of TiO_2 NPs and ZnO NPs on bacterial biofilms (Dharmaraj et al., 2021; Sharma et al., 2022a).

4. Conclusion

The aim of this study was to investigate the efficiency of combinational therapy using two appealing nABs (TiO_2 NPs and ZnO NPs) and antibiotics (amox-clav) against MDR-pathogens. TiO_2 NPs showed higher bacteriostatic activity against *A. baumannii* 80 and *E. coli* 27G, with MIC values of 2 mg/mL and 4 mg/mL for TiO_2 NPs and ZnO NPs, respectively against both MDR-isolates. However, ZnO NPs exhibited higher bactericidal activity, with MDR-isolates death found at 8 mg/mL of ZnO NPs. The results also showed a greater cytotoxicity effect of ZnO NPs compared to TiO_2 NPs in disrupting cell membrane integrity, as assessed by lactate dehydrogenase and Bradford assays. Additionally, ZnO NPs exhibited higher antibiofilm activity. Furthermore, the

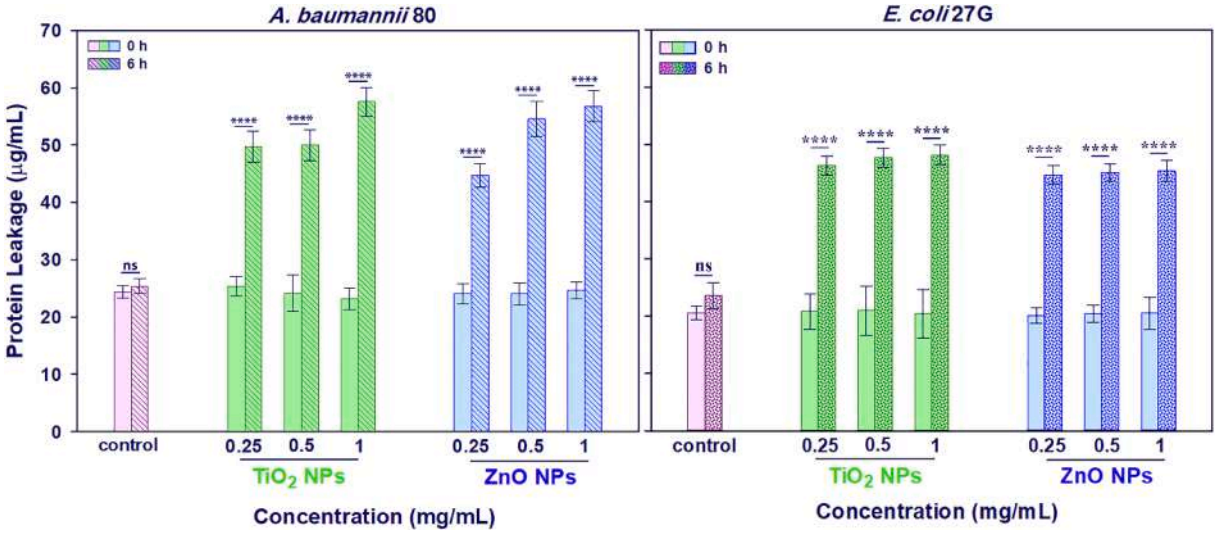

Fig. 10. Bradford assay. The amount of proteins released from *A. baumannii* 80 and *E. coli* 27G exposed to different concentrations of TiO_2 NPs and ZnO NPs. (ns: not significant; **** < 0.0001).

combination of nABs and antibiotics (amox-clav) demonstrated an appropriate synergistic effect, resulting in a significant reduction in the effective dose of antibiotics by 8-fold in the presence of TiO_2 NPs and ZnO NPs.

CRediT authorship contribution statement

Mina Masoudi: Writing – review & editing, Writing – original draft, Visualization, Methodology, Investigation. **Mansour Mashreghi:** Writing – review & editing, Visualization, Validation, Funding acquisition, Conceptualization. **Alireza Zenhari:** Writing – review & editing, Visualization, Project administration, Methodology. **Amir Ala Mashreghi:** Visualization, Writing – review & editing.

Declaration of competing interest

The authors declare that they have no known competing financial interests or personal relationships that could have appeared to influence the work reported in this paper.

Data availability

Data will be made available on request.

Acknowledgment

This work was supported by a grant from Ferdowsi University of Mashhad (grant number: 1/56704).

References

Abbas, S., Uzair, B., Sajjad, S., Leghari, S.A.K., Noor, S., Niazi, M.B.K., Farooq, I., Iqbal, H., 2022. Dual-functional green facile CuO/MgO nanosheets composite as an efficient antimicrobial agent and photocatalyst. Arab. J. Sci. Eng. 47, 5895–5909.

Achudhan, D., Vijayakumar, S., Malaikozhundan, B., Divya, M., Jothirajan, M., Subbian, K., González-Sánchez, Z.I., Mahboob, S., Al-Ghanim, K.A., Vaseeharan, B., 2020. The antibacterial, antibiofilm, antifogging and mosquitocidal activities of titanium dioxide (TiO_2) nanoparticles green-synthesized using multiple plants extracts. J. Environ. Chem. Eng. 8, 104521.

Ahmed, D.S., Mohammed, M.K., 2020. Studying the bactericidal ability and biocompatibility of gold and gold oxide nanoparticles decorating on multi-wall carbon nanotubes. Chem. Pap. 74, 4033–4046.

Ahn, E.-Y., Shin, S.-W., Kim, K., Park, Y., 2022. Facile green synthesis of titanium dioxide nanoparticles by upcycling mangosteen (*Garcinia mangostana*) pericarp extract. Nanoscale Res. Lett. 17, 40.

Alabdali, A., Mahmood, Y., Kzar, M.S., Chinnappan, S., Mani, R.R., Selvaraja, M., Wen, K. J., Sally, L., Kuang, F., 2022. Application of nanoantibiotics approach against anti-bacterial resistance. Int. J. Appl. Pharm. 14, 34–39.

Alavi, M., Karimi, N., Salimikia, I., 2019a. Phytosynthesis of zinc oxide nanoparticles and its antibacterial, antiquorum sensing, antimotility, and antioxidant capacities against multidrug resistant bacteria. J Ind Eng Chem 72, 457–473.

Alavi, M., Karimi, N., Valadbeigi, T., 2019b. Antibacterial, antibiofilm, antiquorum sensing, antimotility, and antioxidant activities of green fabricated Ag, Cu, TiO_2, ZnO, and Fe_3O_4 NPs via protoparmeliopsis muralis lichen aqueous extract against multi-drug-resistant bacteria. ACS Biomater Sci Eng 5, 4228–4243.

Altaf, M., Zeyad, M.T., Hashmi, M.A., Manoharadas, S., Hussain, S.A., Abuhasil, M.S.A., Almuzaini, M.A.M., 2021. Effective inhibition and eradication of pathogenic biofilms by titanium dioxide nanoparticles synthesized using *Carum copticum* extract. RSC Adv 11, 19248–19257.

Baig, U., Ansari, M.A., Gondal, M., Akhtar, S., Khan, F.A., Falath, W., 2020. Single step production of high-purity copper oxide-titanium dioxide nanocomposites and their effective antibacterial and anti-biofilm activity against drug-resistant bacteria. Mater Sci Eng C 113, 110992.

Bakke, R., Olsson, P., 1986. Biofilm thickness measurements by light microscopy. J Microbiol Methods 5, 93–98.

Balaraman, P., Balasubramanian, B., Liu, W.-C., Kaliannan, D., Durai, M., Kamyab, H., Alwetaishi, M., Maluventhen, V., Ashokkumar, V., Chelliapan, S., Maruthupandian, A., 2022. Sargassum myriocystum-mediated TiO_2-nanoparticles and their antimicrobial, larvicidal activities and enhanced photocatalytic degradation of various dyes. Environ Res 204, 112278.

Barani, M., Masoudi, M., Mashreghi, M., Makhdoumi, A., Eshghi, H., 2021. Cell-free extract assisted synthesis of ZnO nanoparticles using aquatic bacterial strains: Biological activities and toxicological evaluation. Int J Pharm 606, 120878.

Cercel, R., Androne, A., Florica, C.S., Lőrinczi, A., Serbschi, C., Baibarac, M., 2023. Nanohybrid composites based on TiO_2 and single-walled carbon nanohorns as promising catalysts for photodegradation of amoxicillin. Molecules 28, 6958.

Chellapandi, T., Madhumitha, G., Roopan, S.M., Elamathi, M., Leeladevi, K., Nagarajan, E., Vadivel, D., Dondi, D., 2023. Construction of ZnO nanoparticles on the layered aluminosilicate Montmorillonite K30 nanocomposite and its enhanced photocatalytic removal performance. Opt Mater 142, 114099.

Chinnathambi, A., Vasantharaj, S., Saravanan, M., Sathiyavimal, S., Duc, P.A., Nasif, O., Alharbi, S.A., Chi, N.T.L., Brindhadevi, K., 2023. Biosynthesis of TiO_2 nanoparticles by *Acalypha indica*; photocatalytic degradation of methylene blue. Appl Nanosci 13, 383–390.

Dar, M.A., Gul, R., Karuppiah, P., Al-Dhabi, N.A., Alfadda, A.A., 2022. Antibacterial activity of cerium oxide nanoparticles against ESKAPE pathogens. Crystals 12, 179.

Das, S., Mukhopadhyay, S., Chatterjee, S., Devi, P.S., Suresh, K.G., 2018. Fluorescent ZnO–Au nanocomposite as a probe for elucidating specificity in DNA interaction. ACS Omega 3, 7494–7507.

Dessai, S., Ayyanar, M., Amalraj, S., Khanal, P., Vijayakumar, S., Gurav, N., Rarokar, N., Kalaskar, M., Nadaf, S., Gurav, S., 2022. Bioflavonoid mediated synthesis of TiO_2 nanoparticles: Characterization and their biomedical applications. Mater Lett 311, 131639.

Dharmaraj, D., Krishnamoorthy, M., Rajendran, K., Karuppiah, K., Jeyaraman, R., Ethiraj, K., 2021. Protein leakage induced marine antibiofouling activity of biosynthesized zinc oxide nanoparticles. J Clust Sci 32, 643–650.

Doğan, S.Ş., Kocabaş, A., 2020. Green synthesis of ZnO nanoparticles with *Veronica multifida* and their antibiofilm activity. Hum Exp Toxicol 39, 319–327.

El-Kahky, D., Attia, M., Easa, S.M., Awad, N.M., Helmy, E.A., 2021. Interactive effects of biosynthesized nanocomposites and their antimicrobial and cytotoxic potentials. Nanomaterials 11, 903.

Eramabadi, P., Masoudi, M., Makhdoumi, A., Mashreghi, M., 2020. Microbial cell lysate supernatant (CLS) alteration impact on platinum nanoparticles fabrication, characterization, antioxidant and antibacterial activity. Mater Sci Eng C 117, 111292.

Fadwa, A.O., Albarag, A.M., Alkoblan, D.K., Mateen, A., 2021. Determination of synergistic effects of antibiotics and ZnO NPs against isolated *E. Coli* and *A. Baumannii* bacterial strains from clinical samples. Saudi J Biol Sci 28, 5332–5337.

Fernando S, Gunasekara T, Holton J. 2018. Antimicrobial nanoparticles: applications and mechanisms of action.

Foschi, M., Marziale, M., Biancolillo, A., 2022. Advanced analytical approach based on combination of FT-IR and Chemometrics for quality control of pharmaceutical preparations. Pharmaceuticals 15, 763.

Gur, T., Meydan, I., Seckin, H., Bekmezci, M., Sen, F., 2022. Green synthesis, characterization and bioactivity of biogenic zinc oxide nanoparticles. Environ Res 204, 111897.

Hadizadeh, M., Toraji, A., 2019. Amoxicillin-loaded polymeric nanoparticles of less than 100 nm: design, preparation and antimicrobial activity against methicillin-resistant *staphylococcus aureus*. Iran J Sci Technol Trans A: Sci 43, 379–386.

Hamk, M., Akçay, F.A., Avcı, A., 2023. Green synthesis of zinc oxide nanoparticles using *Bacillus subtilis* ZBP4 and their antibacterial potential against foodborne pathogens. Prep Biochem Biotechnol 53, 255–264.

Hano, C., Abbasi, B.H., 2021. Plant-based green synthesis of nanoparticles: Production, characterization and applications. Biomolecules 12, 31.

Hutchings, C., Prokocimer Yair, Z., Reifen, R., Shemesh, M., 2021. Antimicrobial effect of zn^{2+} ions governs the microbial quality of donor human milk. Foods 10, 637.

Iqbal, M., Ibrar, A., Ali, A., Memon, F.H., Rehman, F., Bhatti, Z., Soomro, F., Ali, A., Thebo, K.H., 2022. Facile synthesis of zinc oxide nanostructures and their antibacterial and antioxidant properties. Int Nano Lett 12, 205–213.

Jagadeeswar, V., Dhinesh, V., Roopan, S.M., Samuel, E., 2023. Plant extract-mediated synthesis of Ag-doped ZnO: Eco-friendly nanomaterial for environmental restoration, microbial inhibition, cell toxicity, antioxidant potential, and sensing. Colloid J. 85, 827–845.

Jandaghian, F., Pirbazari, A.E., Tavakoli, O., Asasian-Kolur, N., Sharifian, S., 2023. Comparison of the performance of Ag-deposited ZnO and TiO_2 nanoparticles in levofloxacin degradation under UV/visible radiation. J Hazard Mater Adv 9, 100240.

Jasim, N.A., Al-Gasha'a, F.A., Al-Marjani, M.F., Al-Rahal, A.H., Abid, H.A., Al-Kadhmi, N. A., Jakaria, M., Rheima, A.M., 2020. ZnO nanoparticles inhibit growth and biofilm formation of vancomycin-resistant *S. Aureus* (VRSA). Biocatal Agric Biotechnol 29: 101745.

Javed, R., Ain, N.u., Gul, A., Arslan Ahmad, M., Guo, W., Ao, Q., Tian, S., 2022. Diverse biotechnological applications of multifunctional titanium dioxide nanoparticles: An up-to-date review. IET Nanobiotechnol 16, 171–189.

Kanwal, A., Uzair, B., Sajjad, S., Samin, G., Ali Khan, B., Khan Leghari, S.A., Khan Niazi, M.B., Abbas, S., 2022. Synthesis and characterization of carbon dots coated $CaCO_3$ nanocarrier for levofloxacin against multidrug resistance extended-spectrum beta-lactamase *Escherichia coli* of urinary tract infection origin. Microb Drug Resist 28, 106–119.

Kareem, P.A., Alsammak, E.G., Abdullah, Y.J., Bdaiwi, Q.M., 2019. Estimation of antibacterial activity of zinc oxide, titanium dioxide, and silver nanoparticles against multidrug-resistant bacteria isolated from clinical cases in Amara City. Iraq, Drug Invent Today, p. 11.

Khatami, M., Alijani, H.Q., Heli, H., Sharifi, I., 2018. Rectangular shaped zinc oxide nanoparticles: Green synthesis by Stevia and its biomedical efficiency. Ceram Int 44, 15596–15602.

Kiio, T.M., Park, S., 2021. Physical properties of nanoparticles do matter. J Pharm Investig 51, 35–51.

Kumari, A., Singh, A.P., Singh, A.P., 2023. A review on nanoparticles: Smart particles for cancer therapy. In: AIP Conference Proceedings: AIP Publishing.

Lv, Z., Zhong, M., Zhou, Q., Li, Z., Sun, H., Bai, J., Liu, J., Mao, H., 2023. Nutrient strengthening of winter wheat by foliar ZnO and Fe_3O_4 NPs: Food safety, quality, elemental distribution and effects on soil bacteria. Sci Total Environ 893, 164866.

Maalmarugan, J., Ferin, R.Z., Joesna, G., Mustafa, A., Mohamed, M.G., Bououdina, M., Sankar, D., Vimalan, M., SenthilKannan, K., 2022. *In situ* grown ZnO nanoparticles using Begonia leaves–dielectric, magnetic, filter utility and tribological properties for mechano-electronic applications. Appl Phys A 128, 217.

Ma, R., B g, m.s mj, g a, n s., 2019. Anticancer potential of zinc oxide nanoparticles against cervical carcinoma cells synthesized via biogenic route using aqueous extract of *Gracilaria edulis*. Mater. Sci. Eng. C 103, 109840.

Makabenta, J.M.V., Nabawy, A., Li, C.-H., Schmidt-Malan, S., Patel, R., Rotello, V.M., 2021. Nanomaterial-based therapeutics for antibiotic-resistant bacterial infections. Nat Rev Microbiol 19, 23–36.

Mansoor, A., Khan, M.T., Mehmood, M., Khurshid, Z., Ali, M.I., Jamal, A., 2022. Synthesis and characterization of titanium oxide nanoparticles with a novel biogenic process for dental application. Nanomaterials 12, 1078.

Masoudi M, Taghdisi SM, Hashemitabar G, Abnous K. 2023. Targeted co-delivery of FOXM1 aptamer and DOX by nucleolin aptamer-functionalized pH-responsive biocompatible nanodelivery system to enhance therapeutic efficacy against breast cancer: *in vitro* and *in vivo*. Drug Deliv Transl:1-16.

Masoudi, M., Mashreghi, M., Goharshadi, E., Meshkini, A., 2018. Multifunctional fluorescent titania nanoparticles: green preparation and applications as antibacterial and cancer theranostic agents. Artif Cells Nanomed Biotechnol 46, 248–259.

Mehdizadeh, F., Barzegar-Jalali, M., Izadi, E., Osouli-Bostanabad, K., Mohaghegh, S., Shakeri, M.S., Nazemiyeh, H., Omidi, Y., Adibkia, K., 2022. Green and chemical reduction approaches for facile pH-dependent synthesis of gold nanoparticles. Inorg Nano-Met Chem 52, 1396–1404.

Min, T.S., Perveen, N., Khan, N.H., 2020. Comparative purity study by UV spectrophotometric and Fourier-transform infrared spectroscopic (FTIR) techniques for the simultaneous determination of amoxicillin tri-hydrate capsules. Biomed J Sci Technol Res 31, 24219–24235.

Mohammadi R, Massoumi B, Rabani M. 2012. Photocatalytic decomposition of amoxicillin trihydrate antibiotic in aqueous solutions under UV irradiation using Sn/TiO_2 nanoparticles. Int J Photoenergy 2012.

Müller, A.L., Flores, É.M., Müller, E.I., Silva, F.E., Ferrão, M.F., 2011. Attenuated total reflectance with Fourier transform infrared spectroscopy (ATR/FTIR) and different PLS Algorithms for simultaneous determination of clavulanic acid and amoxicillin in powder pharmaceutical formulation. J Braz Chem Soc 22, 1903–1912.

Muthuvel, A., Said, N.M., Jothibas, M., Gurushankar, K., Mohana, V., 2021. Microwave-assisted green synthesis of nanoscaled titanium oxide: photocatalyst, antibacterial and antioxidant properties. J Mater Sci Mater Electron 32, 23522–23539.

Nallal, V.U., Prabha, K., Muthupandi, S., Razia, M., 2022. Synergistic antibacterial potential of plant-based Zinc oxide nanoparticles in combination with antibiotics against *Pseudomonas aeruginosa*. Mater Today: Proc 49, 2632–2635.

Nieto-Maldonado, A., Bustos-Guadarrama, S., Espinoza-Gomez, H., Flores-López, L.Z., Ramirez-Acosta, K., Alonso-Nuñez, G., Cadena-Nava, R.D., 2022. Green synthesis of copper nanoparticles using different plant extracts and their antibacterial activity. J Environ Chem Eng 10, 107130.

Nyoka, M., Choonara, Y.E., Kumar, P., Kondiah, P.P., Pillay, V., 2020. Synthesis of cerium oxide nanoparticles using various methods: implications for biomedical applications. Nanomaterials 10, 242.

Obaidat, R., Al-Ghzawi, B., Al-Taani, B., Al-Shar'i N., 2022. Co-crystallization of amoxicillin trihydrate and potassium clavulanate provides a promising approach for preparation of sustained-release microspheres. AAPS PharmSciTech 23, 131.

Ovais, M., Zia, N., Khalil, A.T., Ayaz, M., Khalil, A., Ahmad, I., 2019. Nanoantibiotics: Recent developments and future prospects. Front Clin Drug Res Anti Infect 5, 158.

Peeters, E., Nelis, H.J., Coenye, T., 2008. Comparison of multiple methods for quantification of microbial biofilms grown in microtiter plates. J Microbiol Methods 72, 157–165.

Rajput, V.D., Chernikova, N., Minkina, T., Gorovtsov, A., Fedorenko, A., Mandzhieva, S., Bauer, T., Tsitsuashvili, V., Beschetnikov, V., Wong, M.H., 2023. Biochar and metal-tolerant bacteria in alleviating ZnO nanoparticles toxicity in barley. Environ Res 220, 115243.

Ribeiro, A.I., Dias, A.M., Zille, A., 2022. Synergistic effects between metal nanoparticles and commercial antimicrobial agents: A review. ACS Appl Nano Mater 5, 3030–3064.

Rossato Viana, A., Godoy Noro, B., Lenz, J., Luiza Machado Teixeira, M., Bolson Serafin, M., Hörner, R., Franco, C., Maria Fontanari Krause, L., Stefanello Vizzotto, B., Jalfim, M.B., 2022. Cytotoxic screening and antibacterial activity of Withaferin A. J Toxicol Environ Health Part A 85, 685–698.

Sajjad, S., Uzair, B., Shaukat, A., Jamshed, M., Leghari, S.A.K., Ismail, M., Mansoor, Q., 2019. Synergistic evaluation of AgO_2 nanoparticles with ceftriaxone against CTXM and blaSHV genes positive ESBL producing clinical strains of Uro-pathogenic *E. coli*. IET Nanobiotechnol 13, 435–440.

Samal, A., Pouthika, K., Rajesh, A., Roopan, S.M., Madhumitha, G., 2024. Photocatalytic degradation and kinetic investigations of ZnO-SnO_2 heterostructures for treatment of methyl violet using non-conventional approach. Inorg Chem Commun 159, 111809.

Sharif, M., Tunio, S.A., Bano, S., 2021. Synergistic effects of Zinc oxide nanoparticles and conventional antibiotics against methicillin resistant *Staphylococcus aureus*. Adv Life Sci 8, 167–171.

Sharma, P., Kumari, R., Yadav, M., Lal, R., 2022a. Evaluation of TiO_2 nanoparticles physicochemical parameters associated with their antimicrobial applications. Indian J Microbiol 62, 338–350.

Sharma, P., Urfan, M., Anand, R., Sangral, M., Hakla, H.R., Sharma, S., Das, R., Pal, S., Bhagat, M., 2022b. Green synthesis of zinc oxide nanoparticles using *Eucalyptus lanceolata* leaf litter: characterization, antimicrobial and agricultural efficacy in maize. Physiol Mol Biol Plants 28, 363–381.

Sharmila, G., Thirumarimurugan, M., Muthukumaran, C., 2019. Green synthesis of ZnO nanoparticles using *Tecoma castanifolia* leaf extract: Characterization and evaluation of its antioxidant, bactericidal and anticancer activities. Microchem. J. 145, 578–587.

Siddique, K., Shahid, M., Shahzad, T., Mahmood, F., Nadeem, H., Saif ur Rehman M, Hussain S, Sadak O, Gunasekaran S, Kamal T., 2021. Comparative efficacy of biogenic zinc oxide nanoparticles synthesized by *Pseudochrobactrum* sp. C5 and chemically synthesized zinc oxide nanoparticles for catalytic degradation of dyes and wastewater treatment. Environ. Sci. Pollut. Res. 28, 28307–28318.

Singh, J., Kaur, S., Kaur, G., Basu, S., Rawat, M., 2019. Biogenic ZnO nanoparticles: A study of blueshift of optical band gap and photocatalytic degradation of reactive yellow 186 dye under direct sunlight. Green Process Synth 8, 272–280.

Songsurang, K., Pakdeebumrung, J., Praphairaksit, N., Muangsin, N., 2011. Sustained release of amoxicillin from ethyl cellulose-coated amoxicillin/chitosan–cyclodextrin-based tablets. AAPS PharmSciTech 12, 35–45.

Sreenivasan, P., Sharma, B., Kaur, S., Rana, S., Biswal, M., Ray, P., Angrup, A., 2022. *In-vitro* susceptibility testing methods for the combination of ceftazidime-avibactam with aztreonam in metallobeta-lactamase producing organisms: Role of combination drugs in antibiotic resistance era. J. Antibiot. 75, 454–462.

Tantisuwanno, C., Dang, F., Bender, K., Spencer, J.D., Jennings, M.E., Barton, H.A., Joy, A., 2021. Synergism between rifampicin and cationic polyurethanes overcomes intrinsic resistance of *Escherichia coli*. Biomacromolecules 22, 2910–2920.

Teixeira, M.C., Carbone, C., Sousa, M.C., Espina, M., Garcia, M.L., Sanchez-Lopez, E., Souto, E.B., 2020. Nanomedicines for the delivery of antimicrobial peptides (AMPs). Nanomaterials 10, 560.

Thakral, F., Bhatia, G.K., Tuli, H.S., Sharma, A.K., Sood, S., 2021. Zinc oxide nanoparticles: from biosynthesis, characterization, and optimization to synergistic antibacterial potential. Curr Pharmacol Rep 7, 15–25.

Thangadurai, D., Sangeetha, J., Prasad, R., 2020. Functional bionanomaterials. Springer.

Tripathi, G., Park, M., Hossain, M., Im, S.B., Lee, B.T., 2022. Fabrication and characterization of cellulose nano crystal and soya modified injectable brushite bone cement for enhanced bone regeneration. Int J Biol Macromol 221, 1536–1544.

Unger, K., Coclite, A.M., 2022. Glucose-responsive boronic acid hydrogel thin films obtained via initiated chemical vapor deposition. Biomacromolecules 23, 4289–4295.

Uyttebroek, S., Chen, B., Onsea, J., Ruythooren, F., Debaveye, Y., Devolder, D., Spriet, I., Depypere, M., Wagemans, J., Lavigne, R., 2022. Safety and efficacy of phage therapy in difficult-to-treat infections: a systematic review. Lancet Infect Dis.

Uzair, B., Akhtar, N., Sajjad, S., Bano, A., Fasim, F., Zafar, N., Leghari, S.A.K., 2020. Targeting microbial biofilms: by *Arctium lappa* l. synthesised biocompatible CeO_2-NPs encapsulated in nano-chitosan. IET Nanobiotechnol 14, 217–223.

Vanamala, K., Tatiparti, K., Bhise, K., Sau, S., Scheetz, M.H., Rybak, M.J., Andes, D., Iyer, A.K., 2021. Novel approaches for the treatment of methicillin-resistant *Staphylococcus aureus*: Using nanoparticles to overcome multidrug resistance. Drug Discov Today 26, 31–43.

Velsankar, K., Sudhahar, S., Parvathy, G., Kaliammal, R., 2020. Effect of cytotoxicity and antibacterial activity of biosynthesis of ZnO hexagonal shaped nanoparticles by *Echinochloa frumentacea* grains extract as a reducing agent. Mater Chem Phys 239, 121976.

Verma, V., Al-Dossari, M., Singh, J., Rawat, M., Kordy, M.G., Shaban, M., 2022. A review on green synthesis of TiO_2 NPs: photocatalysis and antimicrobial applications. Polymers 14, 1444.

Weinstein, M.P., Lewis, J.S., 2020. The clinical and laboratory standards institute subcommittee on antimicrobial susceptibility testing: background, organization, functions, and processes. J Clin Microbiol 58. https://doi.org/10.1128/jcm. 01864-01819.

Yuan, W., Wei, Y., Zhang, Y., Riaz, L., Yang, Q., Wang, Q., Wang, R., 2021. Resistance of multidrug resistant *Escherichia coli* to environmental nanoscale TiO_2 and ZnO. Sci Total Environ 761, 144303.

Zare, M., Namratha, K., Ilyas, S., Sultana, A., Hezam, A., Surmeneva, M.A., Surmenev, R. A., Nayan, M., Ramakrishna, S., Mathur, S., 2022. Emerging trends for ZnO nanoparticles and their applications in food packaging. ACS Food Sci Technol 2, 763–781.

Zhong, N., Zhao, M., Li, Y., 2016. U-shaped, double-tapered, fiber-optic sensor for effective biofilm growth monitoring. Biomed Opt Express 7, 335–351.

Zhou, R., Sui, L., Liu, X., Liu, K., Guo, D., Zhao, W., Song, S., Lv, C., Chen, S., Jiang, T., Cheng, Z., Meng, S., Shan, C., 2023. Multiphoton excited singlet/triplet mixed self-trapped exciton emission. Nat. Commun. 14, 1310.